

1 **A numerical study of convection in rainbands of Typhoon**
2 **Morakot (2009) with extreme rainfall: roles of pressure**
3 **perturbations with low-level wind maxima**

4
5 **Chung-Chieh Wang¹, Hung-Chi Kuo², Richard H. Johnson³, Chun-Yen Lee²,**
6 **Shin-Yi Huang¹, and Yu-Han Chen²**

7 [1]{Department of Earth Sciences, National Taiwan Normal University, Taipei, Taiwan}

8 [2]{Department of Atmospheric Sciences, National Taiwan University, Taipei, Taiwan}

9 [3]{Department of Atmospheric Sciences, Colorado State University, Fort Collins, CO, USA}

10 Correspondence to: Hung-Chi Kuo (kuo@as.ntu.edu.tw)

11
12 **Abstract**

13 This paper investigates the formation and evolution of deep convection inside the east-west
14 oriented rainbands associated with a low-level jet (LLJ) in Typhoon Morakot (2009). With
15 typhoon center to the northwest of Taiwan, the westerly LLJ was resulted from the interaction
16 of typhoon circulation with the southwest monsoon flow, which supplied the water vapor for
17 the extreme rainfall (of ~1000 mm) over southwestern Taiwan. The Cloud-Resolving Storm
18 Simulator with 1-km grid spacing was used to simulate the event, and it successfully
19 reproduced the slow-moving rainbands, the embedded cells, and the dynamics of merger and
20 back-building (BB) on 8 August as observed. Our model results suggest that the intense
21 convection interacted strongly with the westerly LLJ that provided reversed vertical wind
22 shear below and above the jet core. Inside mature cells, significant dynamical pressure
23 perturbations (p'_d) are induced with positive (negative) p'_d at the western (eastern) flank of
24 the updraft near the surface and a reversed pattern aloft (> 2 km). This configuration produced
25 an upward directed pressure gradient force (PGF) to the rear side and favors new development
26 to the west, which further leads to cell merger as the mature cells slowdown in eastward
27 propagation. The strong updrafts also acted to elevate the jet and enhance the local vertical
28 wind shear at the rear flank. Additional analysis reveals that the upward PGF there is resulted
29 mainly by the shearing effect but also by the extension of upward acceleration at low levels.

1 In the horizontal, the upstream-directed PGF induced by the rear-side positive p'_d near the
2 surface is much smaller, but can provide additional convergence for BB development
3 upstream. Finally, the cold-pool mechanism for BB appears to be not important in the
4 Morakot case, as the conditions for strong evaporation in downdrafts do not exist.

5

6 **1 Introduction**

7 **1.1 Literature review**

8 Rainbands develop in response to linear forcing such as fronts, drylines, troughs, and
9 convergence zone (e.g., Carbone, 1982; Browning, 1990; Doswell, 2001; Johnson and Mapes,
10 2001) or by self-organization in a sheared environment (e.g., Bluestein and Jain, 1985;
11 Rotunno et al., 1988; Houze et al., 1990), and are a common type of precipitation systems
12 around the world (e.g., Houze, 1977; Chen and Chou, 1993; Garstang et al., 1994; LeMone et
13 al., 1998; Meng et al., 2013). These linear-shaped mesoscale convective systems (MCSs) are
14 most well studied in mid-latitudes and classified by Parker and Johnson (2000, 2004) into
15 three archetypes based on the location of stratiform region relative to the main line: trailing
16 stratiform (TS), leading stratiform (LS), and parallel stratiform (PS), in response primarily to
17 the different structure of environmental vertical wind shear. Most of these quasi-linear MCSs,
18 especially the TS archetype, are squall lines and propagate relatively fast in direction more-or-
19 less normal to the line (Houze et al., 1990).

20 The above motion of squall-line type systems, however, is not particularly conducive to high
21 rainfall accumulation and the occurrence of flash floods, as Schumacher and Johnson (2005,
22 2006) found that the three archetypes together constitute only about 30% of extreme
23 precipitation events caused by MCSs over the United State Great Plains. For the more
24 hazardous linear systems that travel at small angles to their own alignment (also Dowsell et al.,
25 1996; Brooks and Stensrud, 2000), the above authors further identified two common types of
26 MCSs: the training line-adjointing stratiform (TL/AS) and back-building/quasi-stationary (BB),
27 accounting for about 34% and 20% of the extreme rainfall events, respectively (Schumacher
28 and Johnson, 2005, 2006). Inside the TL/AS type that often forms along or north of a pre-
29 existing slow-moving boundary with an east-west (E-W) orientation, a series of embedded
30 “training” convective cells move eastward (also Stevenson and Schumacher, 2014; Peters and
31 Roebber, 2014). On the other hand, the BB systems are more dependent on mesoscale and

1 storm-scale processes than synoptic boundaries, and while the embedded cells move
2 downwind after initiation, new cells are repeatedly generated at nearly the same location at
3 the upwind side, making the line as a whole “quasi-stationary” (also e.g., Chappell, 1986;
4 Corfidi et al., 1996). Both the above configurations allow for multiple cells to pass through
5 the same area successively, thus rainfall at high intensity to accumulate over a lengthy period
6 (say, several hours) to cause extreme events and related hazards (Doswell et al., 1996). The
7 common mechanism of repeated new cell generation at the end of BB MCSs are through the
8 lifting at the leading edge (i.e., gust front) of the outflow of storm-generated cold pool (see
9 e.g., Fig. 7 of Doswell et al., 1996), which forms on the upwind side of the system (e.g.,
10 Parker and Johnson, 2000; Schumacher and Johnson, 2005, 2009; Houston and Wilhelmson,
11 2007; Moore et al., 2012). Outside the North America, linear MCSs with embedded cells
12 moving along the line are also often responsible for floods, such as the events in France,
13 Australia, Hawaii, and East China (Sénési et al., 1996; Tryhorn et al., 2008; Murphy and
14 Businger, 2011; Luo et al., 2014).

15 Another well-known theory through which the movement of convective cells, and thus the
16 evolution of quasi-linear MCSs, can be modified is the dynamical pressure change induced by
17 the shearing effect in environments with strong vertical wind shear, first put forward by
18 Rotunno and Klemp (1982) to explain the propagation of isolated supercell storms (also e.g.,
19 Weisman and Klemp, 1986; Klemp, 1987). The related diagnostics is also shown to be valid
20 for convection in quasi-linear MCSs by Parker and Johnson (2004). To be detailed in Sect. 3.3,
21 the convective-scale dynamical pressure perturbation (p'_d) can be shown to be roughly
22 proportional to the inner product of the vertical shear vector of horizontal wind (S) and the
23 horizontal gradient of vertical velocity ($\nabla_h w$). Thus, in an environment with westerly vertical
24 shear (S pointing eastward), positive (negative) p'_d is induced to the west (east) of the updraft
25 where $\nabla_h w$ points eastward (westward, see e.g., Fig. 7a of Klemp, 1987). This produces an
26 eastward pressure gradient force (PGF) in the horizontal and favors new updraft development
27 to the east (with $p'_d < 0$ aloft), and helps the storm to propagate forward. In Wang et al.
28 (2009), multiple supercell storms near Taiwan are successfully simulated without the use of
29 initial warm bubbles, and the perturbation pressure (p') couplets (rear-positive and front-
30 negative with respect to S) across the updraft are also reproduced. In the present study, the
31 roles of pressure perturbations associated with convective cells inside the rainband of
32 Typhoon (TY) Morakot in 2009 (e.g., Chien and Kuo, 2011; Wang et al., 2012) are

1 investigated using the simulation results from a cloud-resolving model, and the background
2 related to typhoon rainbands and this particular typhoon is introduced below.

3 **1.2 Typhoon Morakot and back-building rainbands**

4 Located over the western North Pacific (WNP), on average about 3-5 typhoons hit Taiwan
5 annually and pose serious threats to the island. Some of them develop strong interaction with
6 the monsoon that often further enhance the rainfall and worsen the damages. In the past 50
7 years, the most devastating case was TY Morakot in August 2009 (Lee et al., 2011; Chang et
8 al., 2013), leading to 757 deaths and direct damages of roughly 3.8 billion U.S. Dollars
9 (Wang et al., 2012). Based on the Joint Typhoon Warning Center (JTWC) best track, after its
10 formation on 3 August, TY Morakot (2009) approached from the east since 4 August then
11 impacted Taiwan during 6-9 August (Fig. 1a). Embedded inside a 4000-km monsoon gyre
12 that enclosed two other TCs (e.g., Hong et al., 2010; Nguyen and Chen, 2011), Morakot was
13 large in size (Fig. 1a and b) and moved very slowly near Taiwan under the influence of its
14 background environment (e.g., Chien and Kuo, 2011; Wu et al., 2011). During the departure
15 period on 8 August, its mean translation speed further dropped to below 2 m s^{-1} for about 24 h
16 (cf. Fig. 1a), attributed to the effects of asymmetrical latent heating that concentrated at the
17 rear side of the storm over the southern and eastern quadrants (Wang et al., 2012, 2013a; Hsu
18 et al., 2013). At only category 2 on the Saffir-Simpson scale, Moarkot did its destruction
19 almost entirely from the extreme rainfall (e.g., Hendricks et al., 2011) that reached 1624 mm
20 in 24 h, 2361 mm in 48 h, and 2748 mm in 72 (Fig. 2a and b; Hsu et al., 2010) and
21 approached the world record (Table 1). While the above studies clearly indicate that the event
22 of Morakot was resulted from interactions across a wide range of scales, the interplay
23 between TC motion and convection was especially important since the heaviest rainfall over
24 southern Taiwan took place on 8 August when the TC moved the slowest (Figs. 1a and 2a and
25 b, Wang et al., 2012).

26 During 8 August, two types of rainbands appeared persistently over or near Taiwan to cause
27 the extreme rainfall. One was aligned north-south (N-S) near 120.7°E along the windward
28 slopes of southern Central Mountain Range (Figs. 2a-d and 3a, Wang et al., 2012), produced
29 through forced uplift of moisture-laden air by the steep topography at high precipitation
30 efficiency (Yu and Cheng, 2013; Huang et al., 2014). The second type of rainbands, on the
31 other hand, was nearly E-W oriented and parallel to the flow. On 8 August when Morakot's

1 center was over northern Taiwan Strait, these E-W bands formed repeatedly over the southern
2 Taiwan Strait, within the strong low-level convergence zone between the northerly to
3 westerly TC circulation and the monsoonal flow from the southwest, as illustrated in Fig. 3a
4 at 06:00 UTC as an example. Together, the two rainbands formed a “T-shaped” pattern and
5 persisted into 9 August as the TC gradually moved away (Fig. 3b). Similar combinations of
6 topographic (N-S) and TC/monsoon (E-W) rainbands were also observed in several past TCs
7 (Kuo et al., 2010), such as Mindulle (2004), Talim (2005), Haitang (2005), and Jangmi (2008),
8 so it is not unique to Morakot. While some of them have also been noted for evident
9 interaction with the southwesterly monsoon (Chien et al., 2008; Yang et al., 2008; Ying and
10 Zhang, 2012), all are among the 12 most-rainy typhoons in Taiwan, while Morakot (2009) sits
11 at the very top of the list (Chang et al., 2013).

12 The E-W rainbands can be classified as secondary bands (Fig. 3a), as apposed to the three
13 other types of TC rainbands outside the eyewall: principle, connecting, and distant bands
14 (Willoughby et al., 1984; Houze, 2010). Within them, active and vigorous convective cells
15 formed repeatedly off the coast of southwestern Taiwan and further upstream, then moved
16 eastward over land, in a direction parallel to the band and the TC flow (Fig. 4, also Chen et al.,
17 2010; Yu and Cheng, 2013). While several past studies have suggested that supercells may
18 form in TC rainbands (e.g., Eastin and Link, 2009; Morin and Parker, 2011), the multi-
19 cellular structure in Fig. 4 resembles those of both TL/AS and BB types of linear MCSs. An
20 examination of hourly rainfall at gauges with a 24-h total ≥ 700 mm over the southwestern
21 plains on 8 August reveals that at least 84% of the rain came from convective rainfall with an
22 intensity ≥ 20 mm h⁻¹, and the percentage was higher (up to 95%) at sites with higher amount
23 (>1000 mm). Thus, the embedded convection were clearly responsible for the heavy rainfall
24 and serious flooding over much of the coastal plains in southwestern Taiwan (extending
25 inland for about 50 km, roughly west of 120.5°E, cf. Figs. 2a-d and 3). In the examples shown
26 in Fig. 4, back-building and merging and intensification of existing cells were both observed
27 in the E-W bands, and prior to their merger, the new cell to the west often moves faster than
28 the old one. Such behaviors are known to be largely controlled by processes at convective
29 scale. Therefore, besides a favorable forcing of low-level convergence between the TC
30 circulation and southwesterly monsoon at meso- α and β scale to trigger the convection and
31 maintain the rainbands, whether processes at cloud and sub-cloud scale (meso- γ) also

1 contributed in the detailed evolution of convection within the bands to cause the heavy
2 rainfall over southwestern Taiwan? This is the focus of the present study.

3 In the typhoon environment, the maximum wind speed typically occurs near the top of the
4 planetary boundary layer (PBL) due to thermal wind relationship and the influence of surface
5 friction (e.g., Hawkins and Imbembo, 1976; Anthes, 1982, Sect. 2.3). Thus, the vertical wind
6 shear is strongly cyclonic below the level of maximum wind and reverses in direction above it.
7 At 00:00 UTC 8 August, the areal-averaged environmental wind upstream and near southern
8 Taiwan indeed exhibited a distinct west-northwesterly low-level jet (LLJ) reaching 20 m s^{-1} at
9 850 hPa, and the vertical shear below it reversed in direction at 700-200 hPa (Fig. 5a),
10 reminiscent to the “hairpin” shape noted by Schumacher and Johnson (2009). At 06:00 and
11 12:00 UTC (Fig. 5b and c), the LLJ and the associated shear through deep troposphere turned
12 slightly to the left (into more E-W directions), in response to the northwestward movement of
13 Morakot (cf. Fig. 1a). While the LLJ was clearly a part of the TC circulation (e.g., Hence and
14 Houze, 2008), it was most likely enhanced by the southwesterly monsoon (cf. Fig. 3a). Based
15 on Rotunno and Klemp (1982) and Klemp (1987), the interaction between convective updraft
16 and its environmental flow (with LLJ and a reversed wind-shear in profile) would produce an
17 anomalous high to the rear and an anomalous low ahead of the updraft near the surface (below
18 the jet core) but a reversed pattern farther aloft (above the jet core). As illustrated by the
19 schematic in Fig. 6, the effect from such dynamical pressure perturbations would be to favor
20 updraft intensification to the west of mature cells and new development there, i.e., to the back
21 side of the E-W rainbands in our case. Thus, in the present study, we examine such a
22 mechanism and the possible roles played by the pressure perturbations surrounding
23 convective cells in storm evolution (such as back-building and cell merger) mainly through
24 cloud-resolving numerical simulation. In the Morakot case, such meso- γ scale processes and
25 their potential roles in rainfall accumulation have not been studied previously.

26

27 **2 Data and methodology**

28 **2.1 Observational data**

29 The observational data used in this study include standard weather maps, the best-track data
30 from the JTWC, infrared cloud imageries from the geostationary Multifunctional Transport
31 Satellite (MTSAT) of Japan, and data from the rain-gauge network (Hsu, 1998) and radars

1 operated by the Central Weather Bureau (CWB) of Taiwan during our case period. The radar
2 data also include the vertical maximum indicator (VMI) and constant-altitude point position
3 indicator (CAPPI) of reflectivity. Many of the above data have been used in the figures
4 discussed so far.

5 **2.2 Model and experiment**

6 In Wang et al. (2012), the evolution of TY Morakot on 8 August 2009 was simulated in close
7 agreement with the observations using the Cloud-Resolving Storm Simulator (CReSS;
8 Tsuboki and Sakakibara, 2007), with a horizontal grid spacing of 3 km, a dimension of $480 \times$
9 480×50 (vertically stretched grid with spacing $\Delta z = 100\text{-}745$ m), and a model top of 25 km.
10 Using European Center for Medium-range Weather Forecasts (ECMWF) Year of Tropical
11 Convection (YOTC) analyses ($0.25^\circ \times 0.25^\circ$ and 20 levels, every 6 h, e.g., Waliser and
12 Moncrieff, 2007; Moncrieff, 2010) as the initial and boundary conditions (IC/BCs), this
13 particular experiment (their R01 run) served as the control to compare with sensitivity tests
14 designed to examine the effects of asymmetric latent heating on the slow-down of Morakot
15 over the northern Taiwan Strait during its departure. Besides research, the model has also
16 been used to perform real-time forecasts including those for TCs (Wang et al., 2013b; Wang,
17 2014, 2015).

18 For this study, a run similar to R01 was performed with identical setup, except that the model
19 top is increased from 25 to 36 km with slightly reduced vertical resolution. This experiment is
20 referred to as the 3 km run (Table 2) and provides the IC/BCs to a second experiment using a
21 horizontal grid spacing of 1 km and 55 levels, such that detailed structure and evolution of the
22 convective cells embedded inside the rainbands can be reproduced and studied. The
23 integration length of the 1 km run is 24 h starting from 00:00 UTC 8 August 2009, and model
24 output intervals are 7.5 min. The detailed domain configuration and physics of the 3 km and 1
25 km runs are shown in Table 2 (also cf. Figs. 1b and 3a). For later analysis and discussion,
26 only outputs from the 1 km model are used.

27 **2.3 Analysis of pressure perturbations**

28 In this study, to obtain the perturbation pressure p' associated with the convection in the 1 km
29 model results for analysis, two different methods are employed. The first method is to define
30 a background field that varies both with space and time, then separate p' by subtracting the

1 background from the total field. In our case, since the TC center is located to the north and
 2 gradually moving away from the analysis area, set to 22-23°N, 119.2-120.2°E ($1^\circ \times 1^\circ$, cf. Fig.
 3 7a), the accompanying changes, including those with time, need to be partitioned into the
 4 background field. For pressure $p(x, y, z, t)$, its spatial mean over a fixed area is $\bar{p}_A(z, t)$ and
 5 its time average over a period from t_1 to t_2 is $\bar{p}_t(x, y, z)$. The time average of the spatial mean
 6 of p is thus $\bar{p}_{At}(z)$, which varies only with z . Here, we define Δp as the deviation of $\bar{p}_A(z, t)$
 7 from its time average $\bar{p}_{At}(z)$ as

$$8 \quad \Delta p(z, t) = \bar{p}_A(z, t) - \bar{p}_{At}(z). \quad (1)$$

9 Thus, Δp can account for the gradual increase of the areal-mean pressure with time as the TC
 10 moves northward. Containing the averaged spatial pattern plus the change in its mean value
 11 with time, the background pressure (p_0) is defined and computed as

$$12 \quad p_0(x, y, z, t) = \bar{p}_t(x, y, z) + \Delta p(z, t), \quad (2)$$

13 and p' is obtained subsequently as

$$14 \quad p'(x, y, z, t) = p(x, y, z, t) - p_0(x, y, z, t). \quad (3)$$

15 Thus, the background pressure p_0 is not a function of z only, but also varies with location and
 16 time. Here, the time period for analysis is selected to be 03:00-12:00 UTC 8 August. When
 17 needed, the above method is also applied to other variables to obtain their perturbations,
 18 including horizontal wind (u, v) and virtual potential temperature (θ_v).

19 To further examine the detailed roles of pressure perturbation on the development and
 20 evolution of convection, the vertical momentum equation is analyzed and the two components
 21 of p' , the dynamical (p'_d) and buoyancy (p'_b) pressure perturbations (thus $p' = p'_d + p'_b$), are
 22 evaluated following Rotunno and Klemp (1982), Klemp (1987), and Parker and Johnson
 23 (2004). In this second method, p'_d and p'_b and any of their contributing terms can be solved
 24 numerically through the relaxation method by iteration. For better clarity, the relevant
 25 formulation and procedure will be described later in Sects. 3.2 and 3.3, immediately followed
 26 by the results obtained from the 1 km simulation for selected convective cells with the
 27 presence of a westerly wind speed maximum near the top of the PBL in the Morakot case.

28

1 3 Results of model simulation

2 3.1 Model result validation

3 The CReSS model-simulated column maximum mixing ratio of total precipitating
4 hydrometeors (rain + snow + graupel) in the 1 km run over the period of 06:00-08:00 UTC 8
5 August 2009 is shown in Fig. 7, which can be compared with the radar reflectivity composites
6 in Fig. 3 and Wang et al. (2012, their Figs. 6e-g and 7). Comparison of these figures suggests
7 that the model successfully reproduces the rainbands associated with TY Morakot near
8 southwestern Taiwan over this period. On many occasions, more than one roughly E-W
9 aligned bands (as observed) are simulated along a relatively wide zone of low-level
10 convergence between the northerly to westerly TC flow and the west-southwesterly monsoon
11 flow (Fig. 7). These modeled rainbands are in general agreement with earlier observational
12 studies using radars (e.g., Chen et al., 2010; Yu and Cheng, 2013; Wei et al., 2014) while
13 there are often slight displacements in their exact locations, typically by no more than 50 km.
14 Nevertheless, the simulated accumulated rainfall distribution (Fig. 2e-g) compares favorably
15 with the gauge observations on 8 August, including both 00:00-12:00 and 12:00-24:00 UTC
16 (cf. Fig. 2b-d).

17 In the model, convective cells embedded inside the rainbands are repeatedly generated and
18 move eastward after initiation, as in the observation (cf. Fig. 4), and the phenomena of back-
19 building and cell mergers are successfully captured. For example, Fig. 8 shows the
20 development and evolution of several convective cells near 22.5°N using model outputs at
21 1058 m every 7.5 min over 06:30-07:00 UTC. Already mature at the beginning of this 30 min
22 period, cell “A1” moves eastward at an estimated speed of 26.1 m s⁻¹, while cells “B1” and
23 “C1” also travel slightly faster at their mature stage. Meanwhile, new cells, labeled as “A2”,
24 “B2”, and “C2”, respectively, are initiated just upstream (to the west) of each of the three
25 mature cells (Fig. 8), corresponding to back-building behavior as observed (cf. Fig. 4). At
26 early development stage, the new cells also tend to travel faster than the adjacent old cells,
27 most evidently for A2 that reached 31.1 m s⁻¹ and eventually catches up and merges with cell
28 A1 shortly after 07:00 UTC. Thus, the merging behavior of convective cells is also
29 reproduced and linked to the slowing-down of mature cells, with a cycle of roughly 30-40 min
30 in agreement with the observation (cf. Fig. 4). Although Figs. 4 and 8 only show a few

1 selected cells as examples, similar back-building and merging behaviors are quite common
2 both in observations and the 1-km run throughout 8 August (detailed figures not shown).

3 Since cells A1 and A2 exhibit typical evolution in the model with clear merging and back-
4 building behavior, this particular pair of mature-new cells is selected for detailed study.
5 Figure 9 presents the model-simulated horizontal winds and convergence/divergence
6 associated with cell A1 at 547 and 2013 m at 06:30 UTC. While the rainband develops within
7 the low-level convergence zone and the background westerly flow (i.e., the LLJ) increased in
8 speed toward the east (about 35 m s^{-1} at 1058 m near A1; cf. Fig. 7b), the airflow surrounding
9 the mature cell is very different, indicating significant local modulation on the jet by deep
10 convection. Near the surface (Fig. 9a), a wind speed maximum-minimum couplet exists
11 across the updraft (higher wind speed upstream) with a west-southwest-east-northeast (WSW-
12 ENE) orientation and strong deceleration and convergence. At 547 m, the pattern of
13 convergence closely resembles that of vertical motion at 1058 m (cf. Fig. 8, top panel) and
14 extends south and west toward the area of new cell initiation (of A2), mainly due to the
15 deceleration in u -wind and confluence in v -wind, respectively. From 39 to 22 m s^{-1} , the speed
16 convergence in u across A1 at this level is about $5 \times 10^{-3} \text{ s}^{-1}$ and twice the magnitude of the
17 confluence in v , consistent with the deep convection (Fig. 9a). On the other hand, the
18 divergence at 547 m is generally located east and southeast (SE) of the updraft. At 2013 m
19 (Fig. 9b), the updraft core appears slightly to the east and thus is tilted downstream, while the
20 wind speed couplet turns slightly to a SW-NE alignment with similar convergence (from ~ 45
21 to 29 m s^{-1}).

22 In the E-W vertical cross-section along 22.5°N , which slices through (or near) several cells
23 including C1, A1, and B1 at 06:30 UTC (near 119.5 , 119.75 , and 120.05°E , respectively, cf.
24 Figs. 7b and 8), the local deceleration of westerly winds and convergence across convective
25 cells at low levels are evident, while the oncoming environmental flow clearly has the
26 structure of a LLJ with increased speed downstream and a core near 1 km in altitude (Fig.
27 10a). Away from the jet core level, the wind speed decreases much more rapidly below than
28 above, suggesting strong westerly vertical wind shear near the surface ($>10^{-2} \text{ s}^{-1}$ in vorticity)
29 but weak easterly shear above the LLJ, in agreement with Fig. 5. Across the u -wind couplets,
30 the maximum speed typically occurs near 2 km, indicating an upward transport of momentum
31 of the jet by the updraft, and the minimum speed is toward the surface. Another cross-section
32 (about 2 km north) that cuts through the center of A1 (cf. Fig. 8) is shown in Fig. 10b and

1 provides a close-up view of this mature cell, whose updraft indeed tilts eastward (downwind)
 2 with height (also Wei et al., 2014). Inside the updraft, air parcels accelerate upward to reach
 3 near 20 m s^{-1} at mid-levels and this clearly contributes to the strong low-level convergence,
 4 and thus the wind speed couplet, through continuity. Due to the eastward tilt of the updraft,
 5 maximum precipitation and near-surface downdraft (below 2 km) both occur slightly
 6 downwind (Fig. 10b; cf. Fig. 8). This is also depicted in Fig. 11, which in addition confirms
 7 only small surface temperature variations, within 0.5 K, over the rainfall area (centered near
 8 119.77°E). Thus, the cold pool is very weak (cf. Yu and Chen, 2011) and the induced outflow
 9 cannot reach the vicinity of A2 (Fig. 11). These figures suggests that locally, the evaporative
 10 cooling in the downdraft (reflected by a downward decrease in hydrometeors) is barely
 11 enough to overcome the adiabatic warming effect, since the near-surface air is very moist
 12 (close to saturation) and a mid-level drier layer is also lacking in typhoon environment. Thus,
 13 the cold-pool mechanism commonly seen in mid-latitudes to initiate new cells (Doswell et al.,
 14 1996) does not seem important in our case here. Nevertheless, from Figs. 8-10, we see that the
 15 model cells, especially the mature ones, are moving at speeds slower than their low-level
 16 background flow, and we focus on the possible roles played by the pressure perturbations at
 17 sub-cloud scale in merging and back-building behaviors. Below, the vertical momentum
 18 equation is analyzed.

19 **3.2 Analysis of vertical momentum equation**

20 Following Rotunno and Klemp (1982) and Klemp (1987), the three-dimensional momentum
 21 equation can be expressed as

$$22 \quad \frac{d\mathbf{v}}{dt} + \frac{1}{\rho} \nabla p = -g\hat{\mathbf{k}} - f\hat{\mathbf{k}} \times \bar{\mathbf{v}} + \mathbf{F}^*, \quad (4)$$

23 where $\mathbf{v}(u, v, w)$ is the velocity vector, ρ is air density, g is gravitational acceleration, f is the
 24 Coriolis parameter, $\hat{\mathbf{k}}$ the unit vector in z direction, and $\mathbf{F}^* (F_x^*, F_y^*, F_z^*)$ the frictional term.
 25 Both p and ρ can be separated into the background and perturbation (i.e., $p = p_0 + p'$ and $\rho =$
 26 $\rho_0 + \rho'$, note that p_0 here is not the same as the one given in Eq. 2) and the former is assumed
 27 to be in geostrophic and hydrostatic equilibrium. At convective scale, the Coriolis force is
 28 neglected and friction is replaced by a turbulent mixing term $\mathbf{F} (F_x, F_y, F_z)$. Thus, the
 29 horizontal acceleration is caused by the perturbation PGF and turbulent mixing as

$$1 \quad \frac{d\mathbf{v}_h}{dt} = -\frac{1}{\rho} \nabla_h p' + F_x + F_y, \quad (5)$$

2 where the subscript h denotes the horizontal components, while the vertical acceleration
3 (dw/dt) can be approximated as

$$4 \quad \frac{dw}{dt} = -\frac{1}{\rho} \frac{\partial p'}{\partial z} - \frac{\rho'}{\rho} g + F_z \approx -\frac{1}{\rho_0} \frac{\partial p'}{\partial z} - \frac{\rho'}{\rho_0} g + F_z = -\frac{1}{\rho_0} \frac{\partial p'}{\partial z} + B + F_z, \quad (6)$$

5 where $B = -g(\rho'/\rho_0)$ is the buoyancy acceleration. Thus, the vertical acceleration is driven by
6 an imbalance among the perturbation PGF, buoyancy, and turbulent mixing.

7 The buoyancy B is composed of effects from gaseous phase and condensates, and the former
8 can be accounted for by the virtual potential temperature perturbation (θ_v' , where $\theta_v = \theta_{v0} +$
9 θ_v') and the latter is the drag by cloud particles and precipitation, such that

$$10 \quad B = -\frac{\rho'}{\rho_0} g = g \frac{\theta_v'}{\theta_{v0}} - g(q_c + q_i + q_r + q_s + q_g), \quad (7)$$

11 where $q_c, q_i, q_r, q_s,$ and q_g are mixing ratios of cloud water, cloud ice, rain, snow, and graupel,
12 respectively, and available from model outputs. The separation of θ_{v0} and θ_v' is performed
13 using the same method described in Sect. 2.3. Using $p' = p'_d + p'_b$, Eq. (6) can be rewritten to
14 divide the perturbation PGF into two separate terms as

$$15 \quad \frac{dw}{dt} = \frac{\partial w}{\partial t} + u \frac{\partial w}{\partial x} + v \frac{\partial w}{\partial y} + w \frac{\partial w}{\partial z} = -\frac{1}{\rho_0} \frac{\partial p'_d}{\partial z} - \left(\frac{1}{\rho_0} \frac{\partial p'_b}{\partial z} - B \right) + F_z. \quad (8)$$

16 Here, the equation of total derivative is used, and the vertical acceleration is driven by the
17 dynamical perturbation PGF, the buoyancy effect (which contains both the buoyancy
18 perturbation PGF and buoyancy acceleration), and turbulent mixing.

19 **3.3 Analysis of dynamical and buoyancy pressure perturbations**

20 Through the use of nearly incompressible Poisson equation, Rotunno and Klemp (1982) and
21 Klemp (1987) can obtain p'_d and p'_b as the following. First, Eqs. (5) and (6) in Sect. 3.2 can
22 be combined as

$$23 \quad \frac{\partial \mathbf{v}}{\partial t} + \mathbf{v} \cdot \nabla \mathbf{v} + \frac{1}{\rho_0} \nabla p' = B \hat{\mathbf{k}} + \mathbf{F}, \quad (9)$$

24 and the anelastic continuity equation is

1 $\nabla \cdot \rho_0 \mathbf{v} = 0.$ (10)

2 When Eq. (9) is multiplied through by ρ_0 then applied the three-dimensional gradient operator,
 3 the first lhs term vanishes using Eq. (10), and the dynamical and buoyancy terms can be
 4 separated as

5 $\nabla^2 p'_b = \frac{\partial}{\partial z}(\rho_0 B)$ and (11)

6 $\nabla^2 p'_d = -\nabla \cdot (\rho_0 \mathbf{v} \cdot \nabla \mathbf{v}) + \nabla \cdot (\rho_0 \mathbf{F}).$ (12)

7 After expansion and cancellation of terms with friction omitted, Eq. (12) can be rewritten as

8
$$\nabla^2 p'_d = -\rho_0 \left[\underbrace{\left(\frac{\partial u}{\partial x} \right)^2}_{\text{EX1}} + \underbrace{\left(\frac{\partial v}{\partial y} \right)^2}_{\text{EX2}} + \underbrace{\left(\frac{\partial w}{\partial z} \right)^2}_{\text{EX3}} - \underbrace{w^2 \frac{\partial^2}{\partial z^2} (\ln \rho_0)}_{\text{EX4}} \right] - 2\rho_0 \left(\underbrace{\frac{\partial v}{\partial x} \frac{\partial u}{\partial y}}_{\text{SH1}} + \underbrace{\frac{\partial u}{\partial z} \frac{\partial w}{\partial x}}_{\text{SH2}} + \underbrace{\frac{\partial v}{\partial z} \frac{\partial w}{\partial y}}_{\text{SH3}} \right)$$
 (13)

9

10 where the first rhs term inside the brackets is the fluid extension term and the second is the
 11 shearing term. Together, Eqs. (11) and (13) are the Poisson equations of p'_d and p'_b , and a
 12 maximum (minimum) in laplacian corresponds to a minimum (maximum) in pressure
 13 perturbation. From Eq. (11), it can be seen that p'_b is related to the vertical gradient of
 14 buoyancy B . While a variety of processes in Eq. (13) can lead to the change in p'_d , the fluid
 15 extension effect includes four terms: three terms from divergence/convergence and the fourth
 16 term linked to w and the vertical gradient of ρ_0 (and will be referred to as EX1, EX2, EX3,
 17 and EX4, respectively). The fluid shearing effect consists of three terms related to horizontal
 18 wind shear and vertical shear of u and v , respectively (referred to as SH1, SH2, and SH3), and
 19 SH2 and SH3 contain the shearing effect (of $\mathcal{S} \cdot \nabla_h w$) mentioned in Sect. 1.1. After $\nabla^2 p'_b$,
 20 $\nabla^2 p'_d$, or any of its rhs terms is obtained using Eq. (11) or (13), the relaxation method is used
 21 to solve the associated pressure perturbation through iteration.

22 The results of $\nabla^2 p'$ obtained by the two different methods are compared in Fig. 12 at 547 m at
 23 06:30 UTC 8 August as an example. The patterns are generally very similar, with positive
 24 $\nabla^2 p'$ (implying $p' < 0$) to the east and negative $\nabla^2 p'$ (implying $p' > 0$) to the west of mature
 25 cells (e.g., A1 and B1) or positive $\nabla^2 p'$ at and to the south-southeast (SSE) of rising motion of
 26 developing cells and negative $\nabla^2 p'$ to the north-northwest (NNW, e.g., A2, B2, and C1). This
 27 suggests that the separation method described in Sect. 2.3 also gives reasonable results.
 28 However, the contrast between positive and negative $\nabla^2 p'$ values obtained from Eqs. (11) and

1 (13) tends to be slightly larger. A comparison between Fig. 12b with patterns of $\nabla^2 p'_b$ and
2 $\nabla^2 p'_d$ indicates that p' is dominated by p'_b (i.e., p'_d is minimal) in most area (where w is small)
3 except near strong updrafts and downdrafts (not shown).

4 In Fig. 13, a closer view of the model-simulated vertical velocity w , the total pressure
5 perturbation p' obtained through background separation and relaxation method, as well as p'_d
6 through relaxation method at (or near) three different heights of 550, 1050, and 2050 m near
7 cell A1 for the time at 06:30 UTC are shown, together with horizontal winds and vertical
8 wind shear vector S . Again, from the separation method, areas of $p' < 0$ at these three levels
9 are typically found to the southern quadrants of the cell where ascending motion often also
10 appears, while $p' > 0$ is generally to the north and weaker (Fig. 13a, d and g). The peak value
11 of $p' < 0$ near the updraft is roughly -1 hPa, and located to its SE at 550 m but to the
12 southwest at 2050 m. The patterns of total p' solved by the relaxation method at the three
13 levels are generally similar, with $p' < 0$ to the SE and south of the updraft and $p' > 0$ to the
14 north and northwest (NW, Fig. 13b, e and h). However, the N-S difference in p' surrounding
15 the cell is considerably larger (near 3 hPa inside the plotting domain) to give a lower value in
16 minimum p' (~ -1.5 hPa). The reason for this is most likely two fold: (1) the variation in
17 background pressure p_0 on the xy -plane at 06:30 UTC is larger than the time mean used, so
18 that p' centers are under-estimated for this time using the separation method, and (2) the
19 frictional effect that tends to reduce the contrast in p' is not taken into account in Eqs. (11)-
20 (13), causing some over-estimation in p' from the relaxation method. In agreement with
21 earlier discussion (cf. Fig. 10a), the vertical shear across the updraft at 550 m is northwesterly
22 to westerly and quite strong (roughly $1-2 \times 10^{-2} \text{ s}^{-1}$, Fig. 13c) and a clear couplet in p'_d can be
23 found with $p'_d > 0$ to the NW and $p'_d < 0$ to the SE of the updraft, which can already reach
24 about 5 m s^{-1} at this level (cf. Fig. 10b). Consistent with the gradual veering of environmental
25 wind with height in the lower troposphere (cf. Figs. 5b and 13a, d and g) the vertical shear
26 turns clockwise at 1050 and 2050 m, and the alignment of the high-low couplet in p'_d also
27 gradually changes into NNW to SSE and even north-northeast to south-southwest (Fig. 13f
28 and i). Although the vertical shear near 1-2 km is considerably weaker (mostly $< 1 \times 10^{-2} \text{ s}^{-1}$)
29 than at 500 m, the larger w and its horizontal gradient allow for a comparable magnitude in
30 p'_d (cf. Fig. 10b). Thus, the patterns of p'_d up to 2 km are consistent with the SH2 and SH3
31 terms in Eq. (13) and our hypothesis, and with a difference of about 0.6-1 hPa across the high-

1 low couplet, the dynamical pressure perturbations can account for a large part of the
2 difference in total p' near the updraft (Fig. 13).

3 In Fig. 10a, it is seen that deep convection can locally modify the vertical wind profile and
4 change the structure of the LLJ, so here we examine such changes and the resultant effect on
5 the shearing term in Eq. (13) in greater detail before further discussion on the pressure
6 perturbations due to different terms. In Fig. 14, the E-W vertical cross sections as in Fig. 10b
7 (along 22.52°N) but for kinematic variables, vertical wind shear, and $\nabla^2 p'_d$ from SH2 are
8 presented. In Fig. 14a, it can be clearly seen that the low-level convergence induced by the
9 mature cell A1 also causes the LLJ to accelerate toward the updraft and decelerate beneath the
10 updraft core. The upward transport of momentum inside the updraft (~ 6 km in width),
11 consistent with its eastward tilt with height, also elevates the jet to 2-4 km. Due to the
12 formation of the tilted maximum-minimum wind couplet (Fig. 14a), the vertical wind shear
13 directly below the updraft core is enhanced (near 119.71 - 119.75°E and below 1 km, Fig. 14b).
14 Associated with the rise of the LLJ, the northwesterly shear above the jet core at the western
15 flank of the updraft (near 119.72° , 2-4 km) is also strengthened to some extent. In response to
16 this profile of vertical wind shear modified by convection, the pattern of $\nabla^2 p'_d$ from SH2
17 (multiplied by -1 to have the same sign as p'_d) exhibits positive p'_d below 1-1.5 km to the
18 west and negative p'_d below ~ 3 km to the east of the updraft center, and a reversed pattern
19 above to at least 5 km (Fig. 14b), again consistent with our hypothesis.

20 Figure 15 presents the total p' from background separation and p'_b and p'_d and the major
21 contributing terms of p'_d from the relaxation method along the same E-W vertical cross-
22 section as Fig. 14, in addition to w . The total p' associated with cell A1 obtained from the two
23 different methods have similar patterns on the vertical plain (Fig. 15a and b), with largest
24 negative p' of about -1 hPa near 3-4 km and higher p' at the surface immediately to the west
25 of the updraft core. Directly underneath the updraft and to its east, on the other hand, p'
26 obtained through the relaxation method is smaller (more negative) near the surface, which is
27 mainly due to the effects of p'_b rather than p'_d (Fig. 15c and d). To the west of the updraft,
28 however, p'_d is the main reason for the total p' to become positive near the surface and
29 negative further aloft as expected (Fig. 15a-c), and the major contributing terms to this pattern
30 is the shearing and divergent effects of the updraft (SH2 + EX3, Fig. 15e and f), in agreement
31 with Fig. 14. The region of $p'_b < 0$ below and east of the updraft at low levels is resulted from
32 an increase in buoyancy B with height (i.e., $\nabla^2 p'_b > 0$, cf. Eqs. 7 and 11). On this section

1 plane, rhs terms in Eq. (13) other than SH2 and EX3 are much smaller, especially EX4 which
2 is about two orders of magnitude smaller. Thus, these other terms are not shown.

3

4 **4 Discussion**

5 In the previous section, the dynamical pressure perturbation p'_d near the updraft of the mature
6 cell in the rainband is found to exhibit a pattern consistent with our hypothesis, i.e., with
7 positive (negative) perturbation below (above) the LLJ upwind from the updraft, and this
8 pattern is attributed mainly to the shearing effect of the updraft on the vertical wind shear
9 associated with the jet (SH2) but also to the extension term from vertical acceleration inside
10 the tilted updraft (EX3). The induced PGF by the total p' and its components (p'_b and p'_d) in
11 the vertical can be computed using Eq. (8), and this is shown in Fig. 16 on the same cross
12 section through cell A1 (along 22.52°N). With its pattern shown in Fig. 15c, the high-low
13 couplet of p'_d west of the updraft induces an upward-directed PGF there below about 3 km,
14 with a peak value of roughly $7 \times 10^{-2} \text{ m s}^{-2}$ at 1.5 km (Fig. 16a). Such acceleration can
15 produce an upward motion of 5 m s^{-1} under 75 s, or from 5 to 15 m s^{-1} in 150 s across a
16 distance of about 1.5 km, very comparable to the acceleration below the core of the main
17 updraft. Consistent with this result, cell A1 maintains its strength but travels at a slower speed
18 after 0630 UTC (cf. Figs. 8 and 17). Thus, the distribution of p'_d to the rear side of the updraft
19 can certainly affect the evolution of cell A1 and cause it to slow down in moving speed. In
20 other words, the cell merging behavior in the rainbands consisting of multiple cells, when
21 they develop in an environment with an intense LLJ as in the present case, can be explained
22 by the mechanism of dynamical pressure perturbations induced through the shearing (and
23 extension) effect. In Figs. 15 and 16, by strengthening the upward acceleration in the updraft,
24 the shearing effect appears to also act to reinforce the fluid extension term (EX3) in Eq. (13).
25 In addition to its role in cell merger, the reduced propagation speed of mature cells implies an
26 enhancement in low-level convergence upstream. Using Fig. 8 (A1 travelling at 26.1 m s^{-1})
27 and assuming a LLJ of 35 m s^{-1} about 40 km upstream (cf. Figs. 10a), the speed convergence
28 implied is about $2.2 \times 10^{-4} \text{ s}^{-1}$, or $3.2 \times 10^{-4} \text{ s}^{-1}$ larger than the background with speed
29 divergence of $\sim 1 \times 10^{-4} \text{ s}^{-1}$.

30 Because of the surface-based negative p'_b below and east of the updraft, the induced vertical
31 PGF by p'_b is also negative (directed downward) below 3 km (Figs. 15d and 16b), suggesting

1 that the downwind side of the updraft is less favorable for its maintenance and further
2 development. The buoyancy B is mostly positive inside the updraft (Fig. 16c) and this can
3 only come from an increased θ_v' due to latent heat release (cf. Eq. 7). Although B is also
4 positive below the updraft core and even to the west (below 1 km), its values are smaller than
5 the upward acceleration induced by the p'_d pattern and largely cancelled by the effect of p'_b
6 (Fig. 16d). Thus, when all three terms in Fig. 16a-c are added together in Fig. 16e, their total
7 effect on vertical acceleration (cf. Eq. 8) resembles that from the effect of p'_d alone in both the
8 pattern and magnitude (cf. Fig. 16a).

9 The patterns of p' , p'_d , and p'_b , their induced perturbation PGF in the vertical, and B in
10 association with the mature cell, as shown in Figs. 15 and 16, are also quite persistent through
11 time. For example, at 06:45 UTC when A2 grows significantly stronger (cf. Fig. 8), the
12 distributions of p'_d (Fig. 17a) and vertical accelerations from the dynamical (Fig. 17b), total
13 buoyant (Fig. 17c), and their combined effects (Fig. 17d) along the E-W cross section
14 (through A1) all remain similar to those 15 min earlier (cf. Figs. 15c and 16a, d, and e,
15 respectively), although some of them have weakened somewhat. The effects of p'_d ,
16 nevertheless, still dominate over those from p'_b and B at the rear side of cell A1. Similar
17 results are also found in mature cells in other rainbands (not shown).

18 From Fig. 15c and e, the positive p'_d near the surface can be seen to also produce horizontal
19 PGF apart from the vertical PGF, and the westward-directed PGF upstream from A1 (west of
20 119.7°E) can be estimated using Eq. (5) to be about $3\text{-}7 \times 10^{-3} \text{ m s}^{-2}$, which is about one order
21 of magnitude smaller than the PGF in the vertical from p'_d . Nevertheless, a value of 5×10^{-3}
22 m s^{-2} is enough to decelerate the oncoming westerly flow by 1 m s^{-1} in 200 s and induce a
23 speed convergence of roughly $1.4 \times 10^{-4} \text{ s}^{-1}$ (again assuming a background flow of 35 m s^{-1}).
24 Even though this value is one order of magnitude smaller than the convergence associated
25 with cell A2 at 06:30 UTC during its early stage of development ($\sim 1.5 \times 10^{-3} \text{ s}^{-1}$, cf. Fig. 9a)
26 the combined convergence with that implied by a slower moving speed of A1 (as discussed
27 earlier) would be about $4.6 \times 10^{-4} \text{ s}^{-1}$ larger compared to its surrounding. This is certainly not
28 negligible and can provide additional forcing to favor new cell development upstream from
29 the old cell, consistent with the time evolution of A2 (Figs. 8 and 17). Therefore, the role
30 played by the dynamical pressure perturbation in producing an anomalous high near the
31 surface and additional uplift at the rear flank of the updraft of mature cells can favor both
32 merging and new cell initiation further upstream, i.e., the behavior commonly found in back-

1 building MCSs, in the rainbands of TY Morakot (2009) when a strong LLJ is present in the
2 background. Since the LLJ is a common feature in the TC environment, our results are likely
3 also applicable to cell evolution in the rainbands of other TC cases.

4 In the Mei-yu season (May-June), quasi-linear MCSs also often develop near the Mei-yu front
5 in an environment with a LLJ (e.g., Chen, 1992; Chen and Chou, 1993; Chen et al., 2005;
6 Wang et al., 2014), and they may exhibit characteristics reminiscent to the TL/AS or BB
7 systems described by Schumacher and Johnson (2005, 2006) and cause heavy rainfall and
8 flash floods (e.g., Lin et al., 1992; Wang et al., 2005; Jou et al., 2011). Thus, although
9 typhoon rainbands are studied here and the LLJs are typically not as strong in the Mei-yu
10 season, a similar interaction between the updrafts and LLJ may promote cell merging and
11 initiation of new cells upstream, and thus contribute to heavy rainfall and related weather
12 hazards.

13

14 **5 Conclusion and summary**

15 Typhoon Morakot in August 2009 was the most devastating TC to hit Taiwan over the past 50
16 years, with extreme rainfall that came close to the 24 h and 48 h world records. During the
17 period of heaviest rainfall on 8 August, when the TC center was over the northern Taiwan
18 Strait, the E-W oriented, persistent, and slow-moving rainbands and the embedded deep
19 convection that propagated eastward (parallel to the bands) were responsible for the serious
20 and wide-spread flooding over the southwestern plains of Taiwan. Developing inside the low-
21 level convergence zone between the TC vortex (from the N/NW/W) and the monsoon flow
22 (from the WSW/SW) over southern strait, as also observed in several other past TCs, these
23 rainbands were collocated with a westerly LLJ and exhibited frequent cell merging and back-
24 building behavior that contributed to the heavy rainfall. Thus, the possible roles of pressure
25 perturbations associated with deep convection on rainband behavior of TY Morakot (2009)
26 are investigated in this study, mainly through the use of simulation results from the CReSS
27 model at a horizontal grid-spacing of 1 km every 7.5 min.

28 In the model, the rainbands, multiple cells embedded, their eastward movement, and merging
29 and back-building behavior are all successfully captured in close agreement with the
30 observations, although slight positional errors are often unavoidable. In its mature stage, a
31 particular cell at 06:00 UTC 8 August is selected for detailed study. As hypothesized (cf. Fig.
32 6) following Rotunno and Klemp (1982) and Klemp (1987), in an environment of a LLJ (~35

1 m s⁻¹) with reversed vertical wind shear below and above, the interaction between convective
2 updraft and such a vertical shear profile produces a positive dynamical pressure perturbation
3 p'_d to the west (rear) and a negative p'_d to the east of the updraft near the surface (~500 m),
4 but $p'_d < 0$ to the west and $p'_d > 0$ to the east farther aloft above the jet core (> 2 km). At the
5 rear side, the positive-negative couplet of p'_d in the vertical has a difference of about 1 hPa in
6 p , and induces an upward directed PGF whose magnitude is comparable to the acceleration
7 inside the updraft core. This configuration favors updraft development at the rear flank, and
8 subsequently causes the mature cells to slow down and merge with approaching new cells,
9 which remain faster without a strong updraft. The intense updraft of this mature cell, reaching
10 10 m s⁻¹ at 1.3 km and about 20 m s⁻¹ at mid-level, is also found to elevate the jet and act to
11 enhance the local vertical wind shear both above and below the jet core at its rear flank, aided
12 by the induced near-surface convergence at cloud scale.

13 Through the use of relaxation method to solve for each contributing terms of p'_d (and the
14 buoyancy perturbation pressure p'_b , where $p' = p'_d + p'_b$), our results indicate that the above
15 vertical couplet of p'_d to the rear flank is mainly caused by the shearing effect (SH2 in Eq. 13,
16 or $-2\rho_0(\partial u/\partial z)(\partial w/\partial x)$), but also contributed by the vertical extension term (EX3 in Eq. 13, or
17 $-\rho_0(\partial w/\partial z)^2$), i.e., by the upward acceleration in the updraft, at low levels, while the effect of
18 p'_b is nearly counteracted by the buoyancy B in the mature cell examined. Near the surface,
19 the westward-directed horizontal PGF induced by the positive p'_d at the rear side, when
20 combined with the effect from the slow-down of mature cells, can produce an estimated
21 additional convergence (in speed) roughly 1/4-1/3 of the value associated with developing
22 new cell further upstream. Thus, a positive p'_d near the surface in the couplet is also helpful to
23 new cell initiation some distance upstream, i.e., the back-building process, compared to the
24 conditions without a mature cell. Finally, the updraft in the mature cell in our case tilts
25 eastward (downwind) with height due to the presence of the LLJ, and the maximum
26 precipitation and near-surface downdraft occur at the eastern side. However, only a weak cold
27 pool is found since the low-level air is very moist and a dry layer does not exist at mid-levels
28 in the TC environment. Thus, the cold-pool mechanism typical in mid-latitudes to initiate new
29 cells in back-building systems does not appear to be important in our case here.

30

31 *Acknowledgement.* The authors are grateful to the valuable comments from Prof. Russ
32 Schumacher (Colorado State University), Prof. Chris Rozoff (University of Wisconsin-

1 Madison), and an anonymous reviewer that help improve this work. The authors also wish to
2 acknowledge Prof. Ching-Hwang Liu (Chinese Culture University, Taiwan) in providing Fig.
3 4, the Central Weather Bureau (CWB) in providing Fig. 2a and the panels used in Fig. 3b (as
4 well as nearly all observational data), and the assistance from Mr. K.-Y. Chen and Ms. Y.-W.
5 Wang in figure editing. This study is jointly supported by the Ministry of Science and
6 Technology of Taiwan under Grants NSC-102-2119-M-003-003, NSC-103-2119-M-003-001-
7 MY2, MOST 104-2111-M-002-002-MY3, MOST 103-2625-M-002-003, and MOST 103-
8 2111-M-002-010, by the Office of Naval Research Global under Grant N62909-15-1-2008,
9 and by National Taiwan University under Grant NTU-CESRP-104R7064-1.
10

1 **References**

- 2 Anthes, R. A.: Tropical Cyclones. Their Evolution, Structure and Effects. Meteor. Monogr.,
3 No. 41, American Meteorological Society, Boston, MA, USA, 208 pp., 1982.
- 4 Bluestein, H. B., and Jain, M. H.: Formation of mesoscale lines of precipitation: Severe squall
5 lines in Oklahoma during the spring. J. Atmos. Sci., 42, 1711-1732, 1985.
- 6 Brooks, H. E., and Stensrud, D. J.: Climatology of heavy rain events in the United States from
7 hourly precipitation observations. Mon. Weather Rev., 128, 1194-1201, 2000.
- 8 Browning, K. A.: Organization of clouds and precipitation in extratropical cyclones, in:
9 Extratropical Cyclones: The Erik Palmén Memorial Volume, edited by: Newton, C. W. and
10 Holopainen, E. O., Boston, MA, USA, Am. Meteor. Soc., 129-153, 1990.
- 11 Carbone, R. E.: A severe frontal rainband. Part I: Stormwide hydrodynamic structure. J.
12 Atmos. Sci., 39, 258-279, 1982.
- 13 Corfidi, S. F., Meritt, J. H., and Fritsch, J. M.: Predicting the movement of mesoscale
14 convective complexes. Weather Forecast., 11, 41-46, 1996.
- 15 Chang, C.-P., Yang, Y.-T., and Kuo, H.-C.: Large increasing trend of tropical cyclone rainfall
16 in Taiwan and the roles of terrain. J. Climate, 26, 4138-4147, 2013.
- 17 Chappell, C. F.: Quasi-stationary convective events, in: Mesoscale Meteorology and
18 Forecasting, edited by: Ray, P., American Meteorological Society, Boston, MA, USA,
19 289-310, 1986.
- 20 Chen, G. T.-J.: Mesoscale features observed in the Taiwan Mei-Yu season. J. Meteor. Soc.
21 Japan, 70, 497-516, 1992.
- 22 Chen, G. T.-J., and Chou, H.-C.: General characteristics of squall lines observed in TAMEX.
23 Mon. Weather Rev., 121, 726-733, 1993.
- 24 Chen, G. T.-J., Wang, C.-C., and Lin, D. T.-W.: Characteristics of low-level jets over
25 northern Taiwan in Mei-yu season and their relationship to heavy rain events. Mon.
26 Weather Rev., 133, 20-43, 2005.
- 27 Chen, T.-C., Wei, C.-H., Lin, P.-L., and Liou, Y.-C.: The characteristics of radar-observed
28 mesoscale rainbands of Typhoon Morakot, in: Scientific Report on Typhoon Morakot

1 (2009), edited by: Hsu, H.-H., Kuo, H.-C., Jou, J.-D., Chen, T.-C., Lin, P.-H., Yeh, T.-C.,
2 and Wu, C.-C., National Science Council, Taipei, Taiwan, 53-81, (in Chinese), 2010.

3 Chien, F.-C., and Kuo, H.-C.: On the extreme rainfall of Typhoon Morakot (2009). *J.*
4 *Geophys. Res.*, 116, D05104, doi:10.1029/2010JD015092, 2011.

5 Chien, F.-C., Liu, Y.-C., and Lee, C.-S.: Heavy rainfall and southwesterly flow after the
6 leaving of Typhoon Mindulle (2004) from Taiwan. *J. Meteor. Soc. Japan*, 86, 17-41, 2008.

7 Doswell, C. A., III: Severe convective storms—An overview, in: *Severe Convective Storms*,
8 *Meteor. Monogr.*, Boston, MA, USA, edited by: Doswell, C. A. III, ISBN: 978-1-878220-
9 41-7, No. 50, Amer. Meteor. Soc., 1-26, 2001.

10 Doswell, C. A., III, Brooks, H. E., and Maddox, R. A.: Flash flood forecasting: An
11 ingredients-based methodology. *Weather Forecast.*, 11, 560-581, 1996.

12 Eastin, M. D., and Link, M. C.: Miniature supercells in an offshore outer rainband of
13 Hurricane Ivan (2004). *Mon. Weather Rev.*, 137, 2081-2104, 2009.

14 Garstang, M., Massie, H. L., Jr., Halverson, J., Greco, S., and Scala, J.: Amazon coastal squall
15 lines. Part I: Structure and kinematics. *Mon. Weather Rev.*, 122, 608-622, 1994.

16 Guhathakurta, P.: Highest recorded point rainfall over India. *Weather*, 62, p. 349,
17 doi:10.1002/wea.154, 2007.

18 Hawkins, H. F., and Imbembo, S. M.: The structure of a small, intense hurricane—Inez 1966.
19 *Mon. Weather Rev.*, 140, 418-442, 1976.

20 Hence, D. A., and Houze, R. A., Jr.: Kinematic structure of convective-scale elements in the
21 rainbands of Hurricanes Katrina and Rita (2005). *J. Geophys. Res.*, 113, D15108,
22 doi:10.1029/2007JD009429, 2008.

23 Hendricks, E. A., Moskaitis, J. R., Jin, Y., Hodur, R. M., Doyle, J. D., and Peng, M. S.:
24 Prediction and diagnosis of Typhoon Morakot (2009) using the Naval Research
25 Laboratory's mesoscale tropical cyclone model. *Terr. Atmos. Oceanic Sci.*, 22, 579-594,
26 doi:10.3319/TAO.2011.05.30.01(TM), 2011.

27 Holland, G. J.: WMO/TC-No. 560, Report No. TCP-31, World Meteorological Organization;
28 Geneva, Switzerland, 1993.

- 1 Hong, C.-C., Lee, M.-Y., Hsu, H.-H., and Kuo, J.-L.: Role of submonthly disturbance and 40-
2 50 day ISO on the extreme rainfall event associated with Typhoon Morakot (2009) in
3 southern Taiwan. *Geophys. Res. Lett.*, 37, L08805, doi:10.1029/2010GL042761, 2010.
- 4 Houston, A. L., and Wilhelmson, R. B.: Observational analysis of the 27 May 1997 central
5 Texas tornadic event. Part I: Prestorm environment and storm maintenance/propagation.
6 *Mon. Weather Rev.*, 135, 701-726, 2007.
- 7 Houze, R. A., Jr.: Structure and dynamics of a tropical squall-line system. *Mon. Weather Rev.*,
8 105, 1540-1567, 1977.
- 9 Houze, R. A., Jr.: Clouds in tropical cyclones. *Mon. Weather Rev.*, 138, 293-344, 2010.
- 10 Houze, R. A., Jr., Smull, B. F., and Dodge, P.: Mesoscale organization of springtime
11 rainstorms in Oklahoma. *Mon. Weather Rev.*, 118, 613-654, 1990.
- 12 Hsu, H.-H., Kuo, H.-C., Jou, J.-D., Chen, T.-C., Lin, P.-H., Yeh, T.-C., and Wu, C.-C.:
13 Scientific report on Typhoon Morakot (2009), National Science Council, Taipei, Taiwan,
14 192 pp., (in Chinese), 2010.
- 15 Hsu, J.: ARMTS up and running in Taiwan. *Väisälä News*, 146, 24-26, 1998.
- 16 Hsu, L.-H., Kuo, H.-C., and Fovell, R. G.: On the geographic asymmetry of typhoon
17 translation speed across the mountainous island of Taiwan, *J. Atmos. Sci.*, 70, 1006-1022,
18 2013.
- 19 Huang, H.-L., Yang, M.-J., and Sui, C.-H.: Water budget and precipitation efficiency of
20 Typhoon Morakot (2009). *J. Atmos. Sci.*, 71, 112-129, 2014.
- 21 Johnson, R. H., and Mapes, B. E.: Mesoscale processes and severe convective weather.
22 *Severe Convective Storms*, Meteor. Monogr., No. 50, Amer. Meteor. Soc., 71-122, 2001.
- 23 Jou, B. J.-D., Lee, W.-C., and Johnson, R. H.: An overview of SoWMEX/TiMREX and its
24 operation. edited by: Chang, C.-P., Ding, Y., Lau, N.-C., Johnson, R. H., Wang, B., and
25 Yasunari, T., in: *The Global Monsoon System: Research and Forecast*, 2nd edn., World
26 Scientific, Singapore, 303-318, 2011.
- 27 Klemp, J. B.: Dynamics of tornadic thunderstorms. *Annu. Rev. Fluid Mech.*, 19, 369-402,
28 1987.

- 1 Kuo, H.-C., Yang, Y.-T., and Chang, C.-P.: Typhoon Morakot (2009): Interplay of southwest
2 monsoon, terrain, and mesoscale convection. Int. Workshop on Typhoon Morakot (2009),
3 Taipei, Taiwan, National Science Council and National Applied Research Laboratories,
4 Taipei, Taiwan, 25-26 March 2010, p. 55, 2010.
- 5 Lee, C.-S., Wu, C.-C., Chen, T.-C., and Elsberry, R. L.: Advances in understanding the
6 “perfect monsoon-influenced typhoon”: summary from international conference on
7 typhoon Morakot (2009). *Asian-Pacific J. Atmos. Sci.*, 47, 213-222, 2011.
- 8 LeMone, M. A., Zipser, E. J., and Trier, S. B.: The role of environmental shear and
9 thermodynamic conditions in determining the structure and evolution of mesoscale
10 convective systems during TOGA COARE. *J. Atmos. Sci.*, 55, 3493-3518, 1998.
- 11 Lin, Y.-J., Pasken, R. W., and Chang, H.-W.: The structure of a subtropical prefrontal
12 convective rainband. Part I: Mesoscale kinematic structure determined from dual-Doppler
13 measurements. *Mon. Weather Rev.*, 120, 1816-1836, 1992.
- 14 Luo, Y., Gong, Y., and Zhang, D.-L.: Initiation and organizational modes of an extreme-rain-
15 producing mesoscale convective system along a Mei-yu front in East China. *Mon. Weather*
16 *Rev.*, 142, 203-221, 2014.
- 17 Meng, Z., Yan, D., and Zhang, Y.: General features of squall lines in East China. *Mon.*
18 *Weather Rev.*, 141, 1629-1647, 2013.
- 19 Moncrieff, M. W.: The multiscale organization of moist convection and the intersection of
20 weather and climate. *Why Does Climate Vary?*, Geophys. Monogr., Vol. 189, Amer.
21 Geophys. Union, 3-26, 2010.
- 22 Moore, B. J., Neiman, P. J., Ralph, F. M., and Barthold, F. E.: Physical processes associated
23 with heavy flooding rainfall in Nashville, Tennessee, and vicinity during 1-2 May 2010:
24 The role of an atmospheric river and mesoscale convective systems. *Mon. Weather Rev.*,
25 140, 358-378, 2012.
- 26 Morin, M. J., and Parker, M. D.: A numerical investigation of supercells in landfalling
27 tropical cyclones, *Geophys. Res. Lett.*, 38, L10801, doi:10.1029/2011GL047448, 2011.
- 28 Murphy, M. J., Jr., and Businger, S.: Orographic influences on an Oahu flood. *Mon. Weather*
29 *Rev.*, 139, 2198-2217, 2011.

- 1 Nguyen, H. V., and Chen, Y.-L.: High-resolution initialization and simulations of Typhoon
2 Morakot (2009). *Mon. Weather Rev.*, 139, 1463-1491, 2011.
- 3 Parker, M. D., and Johnson, R. H.: Organizational modes of midlatitude mesoscale convective
4 systems. *Mon. Weather Rev.*, 128, 3413-3436, 2000.
- 5 Parker, M. D., and Johnson, R. H.: Structures and dynamics of quasi-2D mesoscale
6 convective systems. *J. Atmos. Sci.*, 61, 545-567, 2004.
- 7 Peters, J. M., and Roebber, P. J.: Synoptic control of heavy-rain-producing convective
8 training episodes. *Mon. Weather Rev.*, 142, 2464-2482, 2014.
- 9 Quetelard, H., Bessemoulin, P., Cervený, R. S., Peterson, T. C., Burton, A., and Boodhoo, Y.:
10 Extreme weather: World-record rainfalls during Tropical Cyclone Gamede. *B. Am.*
11 *Meteorol. Soc.*, 90, 603-608, 2009.
- 12 Rotunno, R., and Klemp, J. B.: The influence of the shear-induced pressure gradient on
13 thunderstorm motion. *Mon. Weather Rev.*, 110, 136-151, 1982.
- 14 Rotunno, R., Klemp, J. B., and Weisman, M. L.: A theory for strong, long-lived squall lines. *J.*
15 *Atmos. Sci.*, 45, 463-485, 1988.
- 16 Schumacher, R. S., and Johnson, R. H.: Organization and environmental properties of
17 extreme-rain-producing mesoscale convective systems. *Mon. Weather Rev.*, 133, 961-976,
18 2005.
- 19 Schumacher, R. S., and Johnson, R. H.: Characteristics of U.S. extreme rain events during
20 1999-2003. *Weather Forecast.*, 21, 69-85, 2006.
- 21 Schumacher, R. S., and Johnson, R. H.: Quasi-stationary, extreme-rain-producing convective
22 systems associated with midlevel cyclonic circulations. *Weather Forecast.*, 24, 555-574,
23 2009.
- 24 S n si, S., Bougeault, P., Ch ze, J.-L., Cosentino, P., and Thepenier, R.-M.: The Vaison-La-
25 Romaine flash flood: Mesoscale analysis and predictability issues. *Weather Forecast.*, 11,
26 417-442, 1996.
- 27 Stevenson, S. N., and Schumacher, R. S.: A 10-year survey of extreme rainfall events in the
28 central and eastern United States using gridded multisensor precipitation analyses. *Mon.*
29 *Weather Rev.*, 142, 3147-3162, 2014.

- 1 Tryhorn, L., Lynch, A., Abramson, R., and Parkyn, K.: On the meteorological mechanisms
2 driving postfire flash floods: A case study. *Mon. Weather Rev.*, 136, 1778-1791, 2008.
- 3 Tsuboki, K., and Sakakibara, A.: Numerical Prediction of High-Impact Weather Systems: The
4 Textbook for the Seventeenth IHP Training Course in 2007. Hydrospheric Atmospheric
5 Research Center, Nagoya University, and UNESCO, Nagoya, Japan. ISBN: 978-4-
6 9980619-8-4, 273 pp., 2007.
- 7 Waliser, D. E., and Moncrieff, M.: Year of tropical convection---A Joint WCRP- THORPEX
8 activity to address the challenge of tropical convection. *GEWEX News*, No. 2,
9 International GEWEX Project Office, Silver Spring, MD, 8-9, 2007.
- 10 Wang, C.-C.: On the calculation and correction of equitable threat score for model
11 quantitative precipitation forecasts for small verification areas: The example of Taiwan.
12 *Weather Forecast.*, 29, 788-798, 2014.
- 13 Wang, C.-C.: The more rain, the better the model performs---The dependency of quantitative
14 precipitation forecast skill on rainfall amount for typhoons in Taiwan. *Mon. Weather Rev.*,
15 143, 1723-1748, 2015.
- 16 Wang, C.-C., Chen, G. T.-J., Chen, T.-C., and Tsuboki, K.: A numerical study on the effects
17 of Taiwan topography on a convective line during the mei-yu season. *Mon. Weather Rev.*,
18 133, 3217-3242, 2005.
- 19 Wang, C.-C., Chen, G. T.-J., Yang, S.-C., and Tsuboki, K.: Wintertime supercell
20 thunderstorms in a subtropical environment: Numerical simulation. *Mon. Weather Rev.*,
21 137, 2175-2202, 2009.
- 22 Wang, C.-C., Kuo, H.-C., Chen, Y.-H., Huang, H.-L., Chung, C.-H., and Tsuboki, K.: Effects
23 of asymmetric latent heating on typhoon movement crossing Taiwan: The case of Morakot
24 (2009) with extreme rainfall. *J. Atmos. Sci.*, 69, 3172-3196, 2012.
- 25 Wang, C.-C., Chen, Y.-H., Kuo, H.-C., and Huang, S.-Y.: Sensitivity of typhoon track to
26 asymmetric latent heating/rainfall induced by Taiwan topography: A numerical study of
27 Typhoon Fanapi (2010). *J. Geophys. Res. Atmos.*, 118, 3292-3308,
28 doi:10.1002/jgrd.50351, 2013a.
- 29 Wang, C.-C., Kuo, H.-C., Yeh, T.-C., Chung, C.-H., Chen, Y.-H., Huang, S.-Y., Wang, Y.-W.,
30 and Liu, C.-H.: High-resolution quantitative precipitation forecasts and simulations by the

1 Cloud-Resolving Storm Simulator (CReSS) for Typhoon Morakot (2009). *J. Hydrol.*, 506,
2 26-41, <http://dx.doi.org/10.1016/j.jhydrol.2013.02.018>, 2013b.

3 Wang, C.-C., Hsu, J. C.-S., Chen, G. T.-J., and Lee, D.-I. : A study of two propagating heavy-
4 rainfall episodes near Taiwan during SoWMEX/TiMREX IOP-8 in June 2008. Part I:
5 Synoptic evolution, episode propagation, and model control simulation. *Mon. Weather*
6 *Rev.*, 142, 2619-2643, 2014.

7 Wei, C.-H., Chuang, Y.-C., Hor, T.-H., Liao, C.-C., and Yeh, N.-C.: Dual-Doppler radar
8 investigation of a convective rainband during the impact of the southwesterly monsoonal
9 flow on the circulation of Typhoon Morakot (2009). *J. Meteor. Soc. Japan*, 92, 363-383,
10 2014.

11 Weisman, M. L., and Klemp, J. B.: Characteristics of isolated convective storms, in:
12 *Mesoscale Meteorology and Forecasting*, edited by: Ray, P. S., Amer. Meteor. Soc.,
13 Boston, MA, USA, 331-358, 1986.

14 Wu, L., Liang, J., and Wu, C.-C.: Monsoonal influence on Typhoon Morakot (2009). Part I:
15 Observational analysis. *J. Atmos. Sci.*, 68, 2208-2221, 2011.

16 Yang, S., Kang, K.-R., Cui, X., and Wang, H.: Diagnostic analysis of the asymmetric
17 structure of the simulated landfalling typhoon “Haitang”. *Prog. Nat. Sci.*, 18, 1249-1260,
18 2008.

19 Ying, Y., and Zhang, Q.: A modeling study on tropical cyclone structural changes in response
20 to ambient moisture variations. *J. Meteor. Soc. Japan*, 90, 755-770, 2012.

21 Yu, C.-K., and Chen, Y.: Surface fluctuations associated with tropical cyclone rainbands
22 observed near Taiwan during 2000-08. *J. Atmos. Sci.*, 68, 1568-1585, 2011.

23 Yu, C.-K., and Cheng, L.-W.: Distribution and mechanisms of orographic precipitation
24 associated with Typhoon Morakot (2009). *J. Atmos. Sci.*, 70, 2894-2915, doi:
25 10.1175/JAS-D-12-0340.1, 2013.

26

1 Table 1. Comparison of maximum accumulated rainfall (mm) observed in TY Morakot (2009)
 2 in Taiwan (Hsu et al., 2010) and the World's record rainfall, including location and date
 3 (source: World Meteorological Organization World Archive of Weather and Climate
 4 Extremes, available at <http://wmo.asu.edu/#global>; Holland, 1993; Guhathakurta, 2007;
 5 Quetelard et al., 2009).

6

Duration	Morakot	World record		
		Amount	Location	Date
24 h	1624	1825	Foc-Foc, La Réunion	7-8 Jan 1966
48 h	2361	2493	Cherrapunji, India	15-16 Jun 1995
72 h	2748	3930	Cratère Commerson, La Réunion	24-26 Feb 2007
96 h	2855	4936	Cratère Commerson, La Réunion	24-27 Feb 2007

7

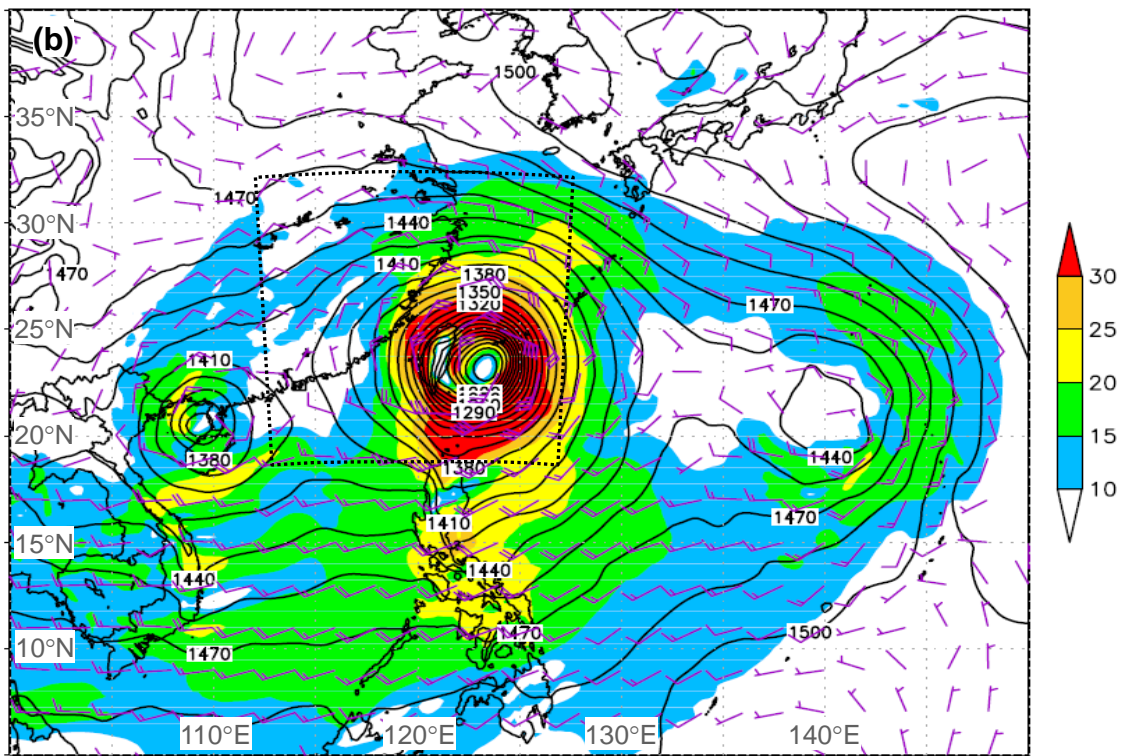
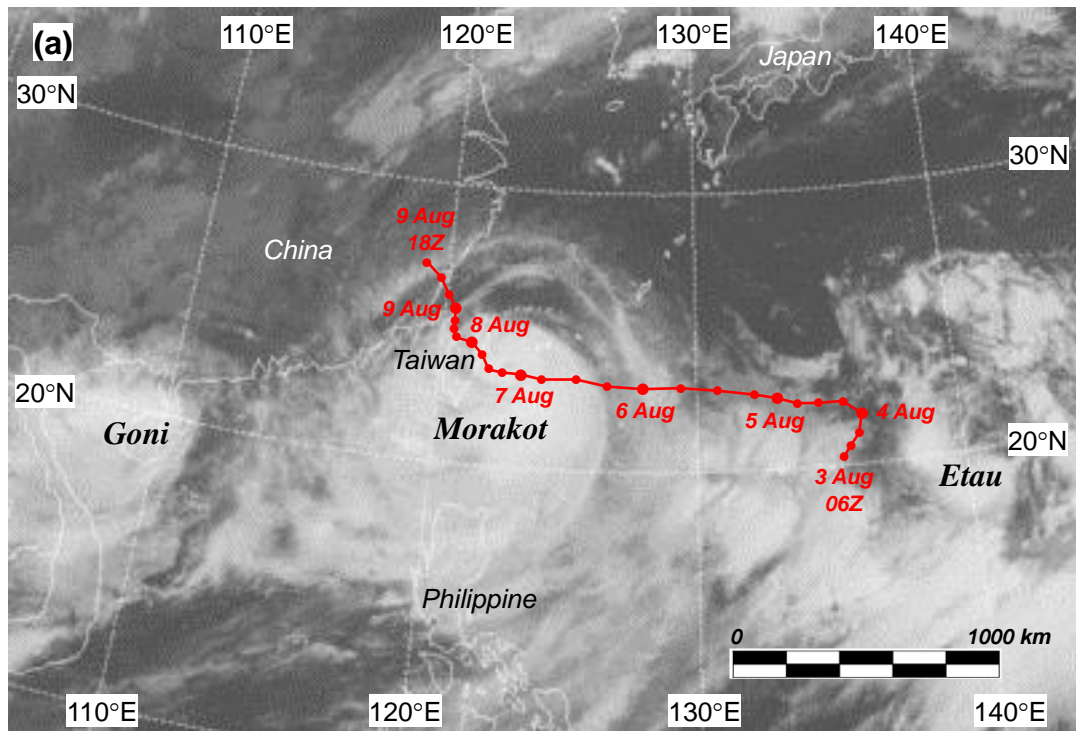
8

1 Table 2. Domain configuration, physics, and experiment design used in this study. In the
 2 vertical, the grid spacing (Δz) of the CReSS model is stretched (smallest at the bottom), and
 3 the averaged spacing is given in the parentheses.

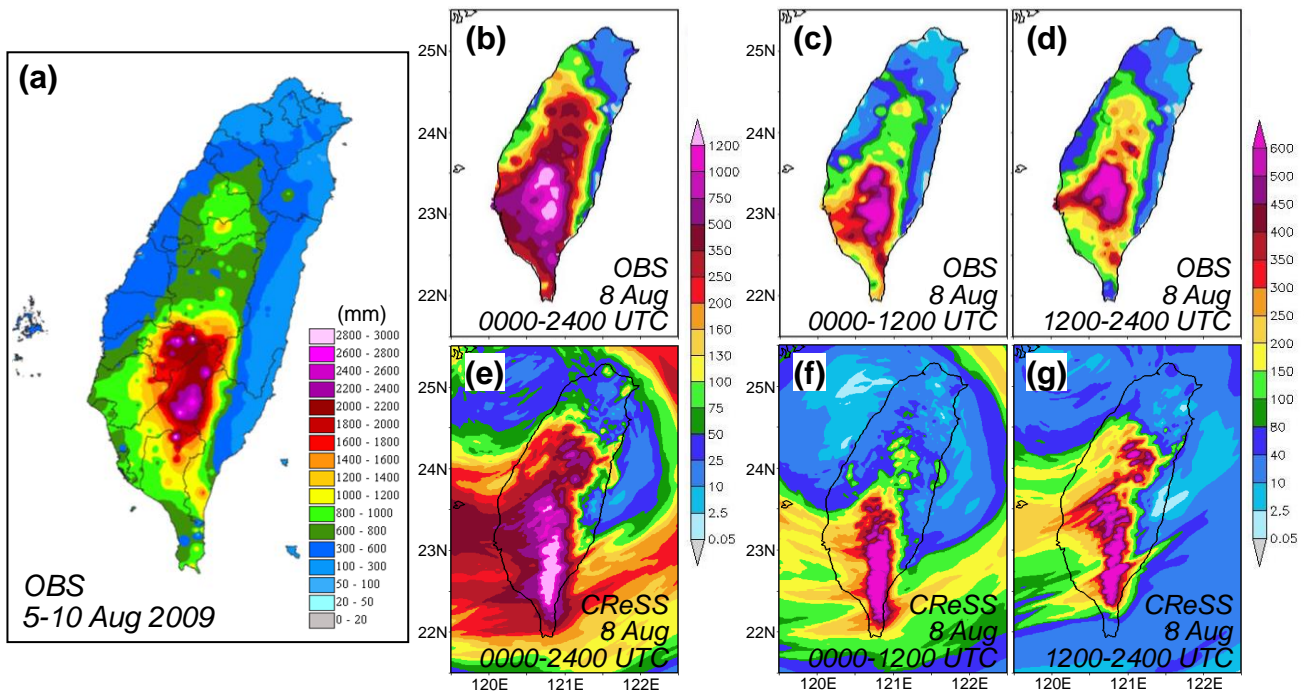
4

	3 km	1 km
Projection	Lambert Conformal, center at 120°E, secant at 10°N and 40°N	
Grid dimension (x, y, z)	480 × 480 × 50	450 × 500 × 55
Grid spacing (km)	3.0 × 3.0 × 0.1-0.98 (0.72)	1.0 × 1.0 × 0.1-0.718 (0.5)
Topography and SST	Real at (1/120)°, and weekly mean at 1° resolution	
Initial/boundary conditions (IC/BCs)	ECMWF YOTC analyses (0.25° × 0.25°, 20 levels, 6 h)	Outputs from 3 km run (3 km, 55 levels, 15 min)
Initial time	0000 UTC 8 Aug 2009	
Integration length	48 h	24 h
Output frequency	15 min	7.5 min
Cloud microphysics	Bulk cold rain scheme (mixed phase with 6 species)	
PBL parameterization	1.5-order closure with TKE prediction	
Surface processes	Energy/momentum fluxes, shortwave and longwave radiation	
Soil model	41 levels, every 5 cm to 2 m deep	

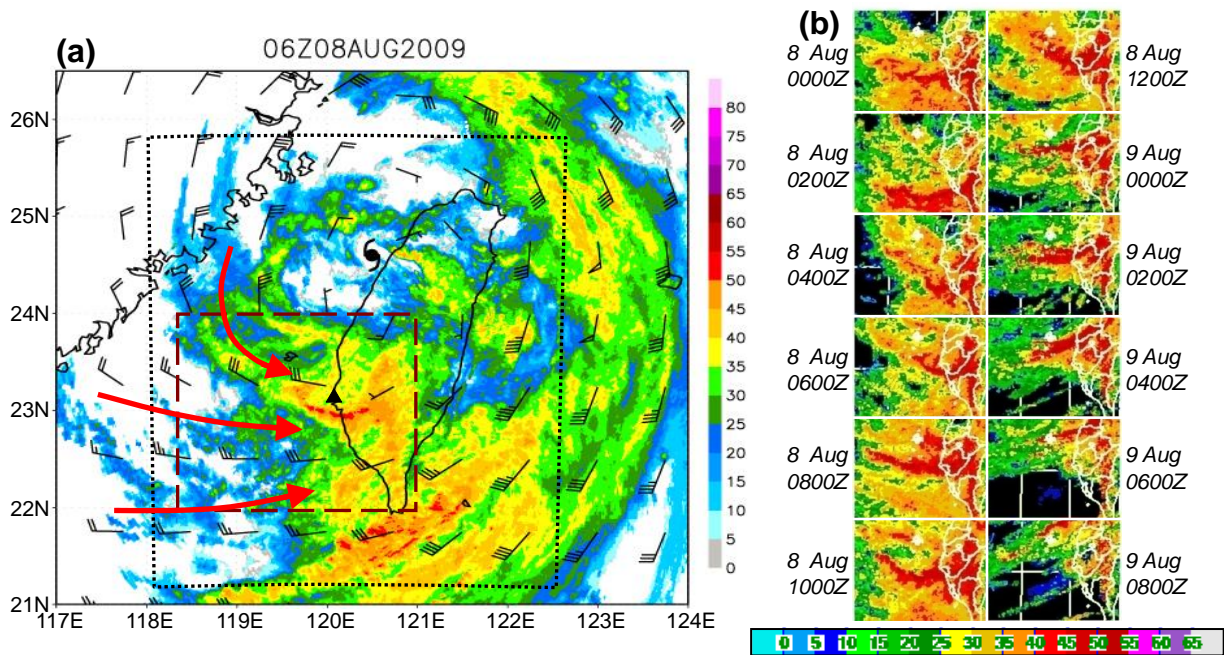
5



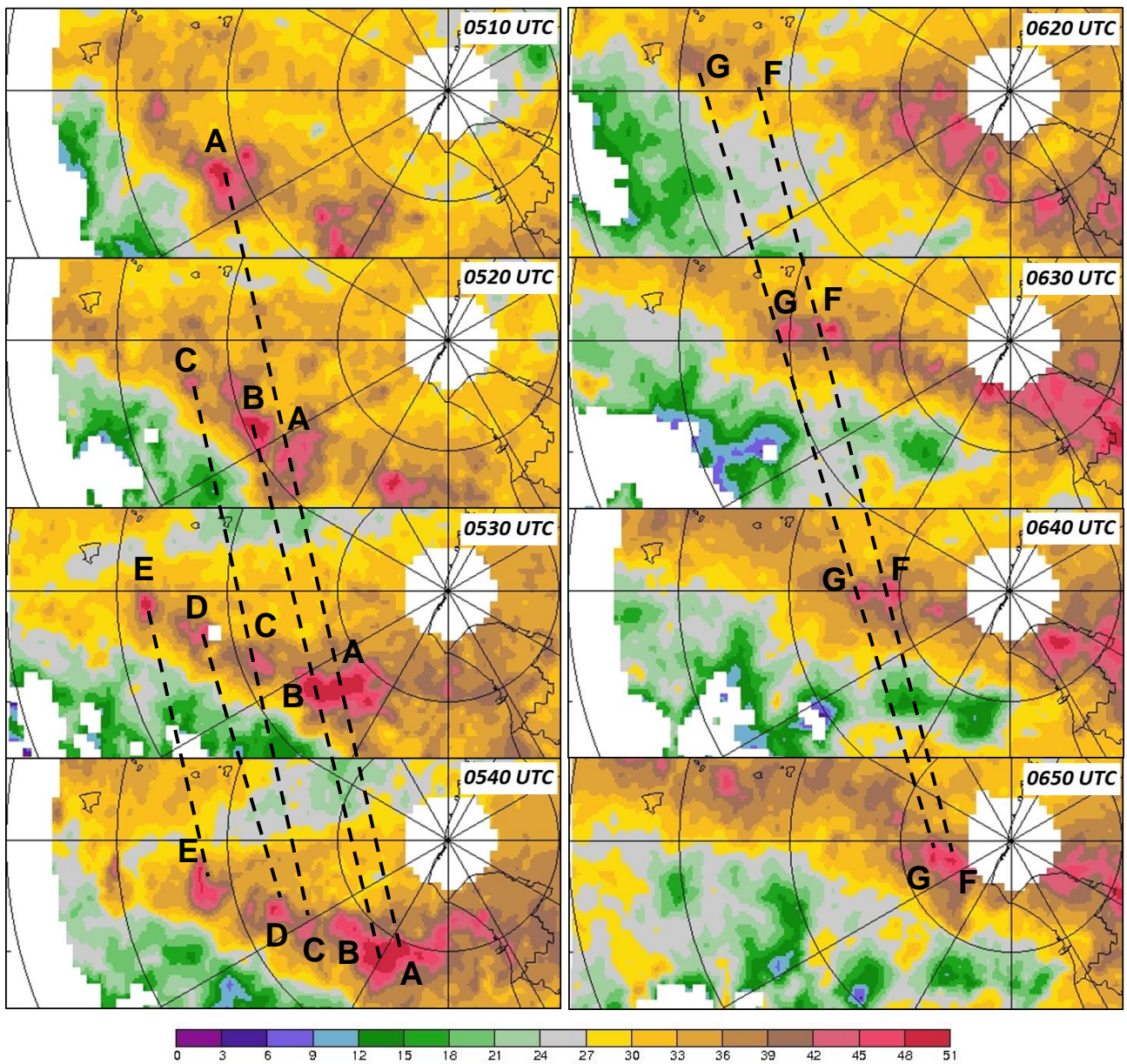
1 Figure 1. (a) The JTWC best-track of Typhoon Morakot (TY0908) overlaid with MTSAT IR
 2 cloud imagery at 00:30 UTC 7 August 2009. The TC positions are given every 6 h. (b) The
 3 ECMWF-YOTC analysis of geopotential height (gpm, contours) and horizontal winds [m s^{-1} ,
 4 full (half) barb = 10 (5) m s^{-1} , wind speed shaded] at 850 hPa at 00:00 UTC 7 August 2009.
 5 The domain of 3 km experiment is also plotted (dotted region).



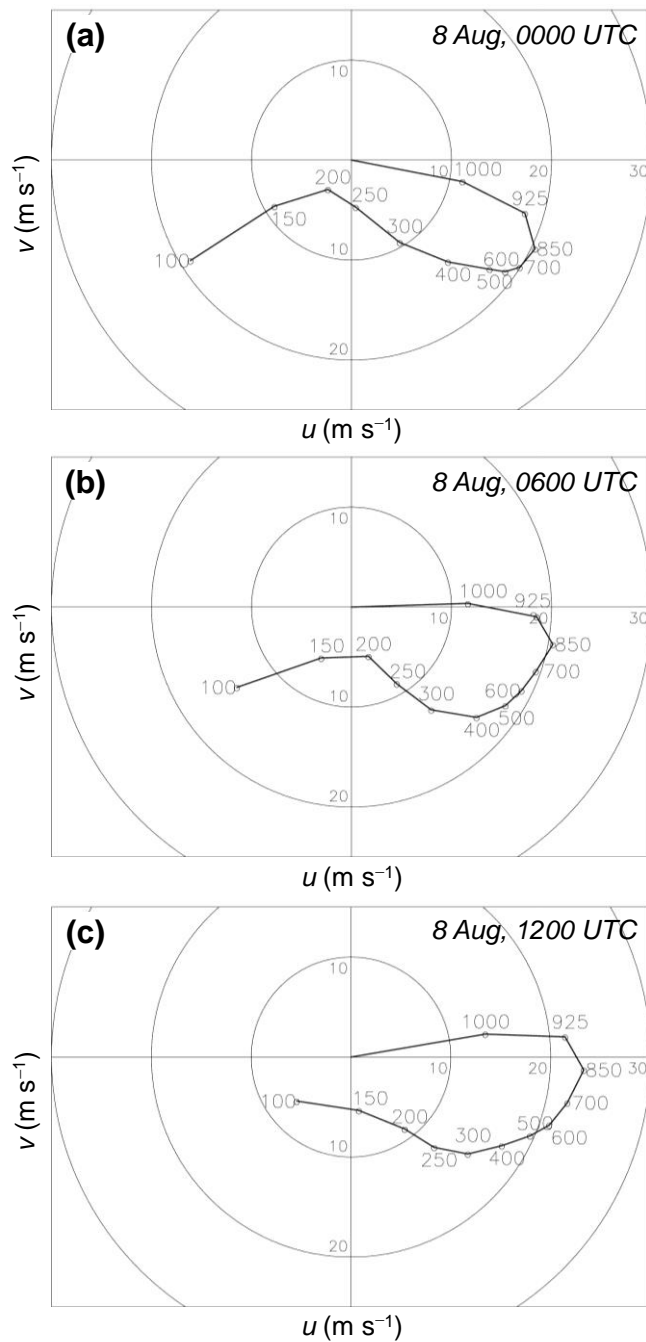
1 Figure 2. Observed (a) total rainfall distribution (mm) in Taiwan over 5-10 August, (b) daily
 2 (00:00-24:00 UTC) rainfall distribution on 8 August, and 12 h rainfall over (c) 00:00-12:00
 3 UTC and (d) 12:00-24:00 UTC on 8 August, during Morakot (2009). (e-g) Same as (b-d)
 4 except from 1 km CReSS model simulation.



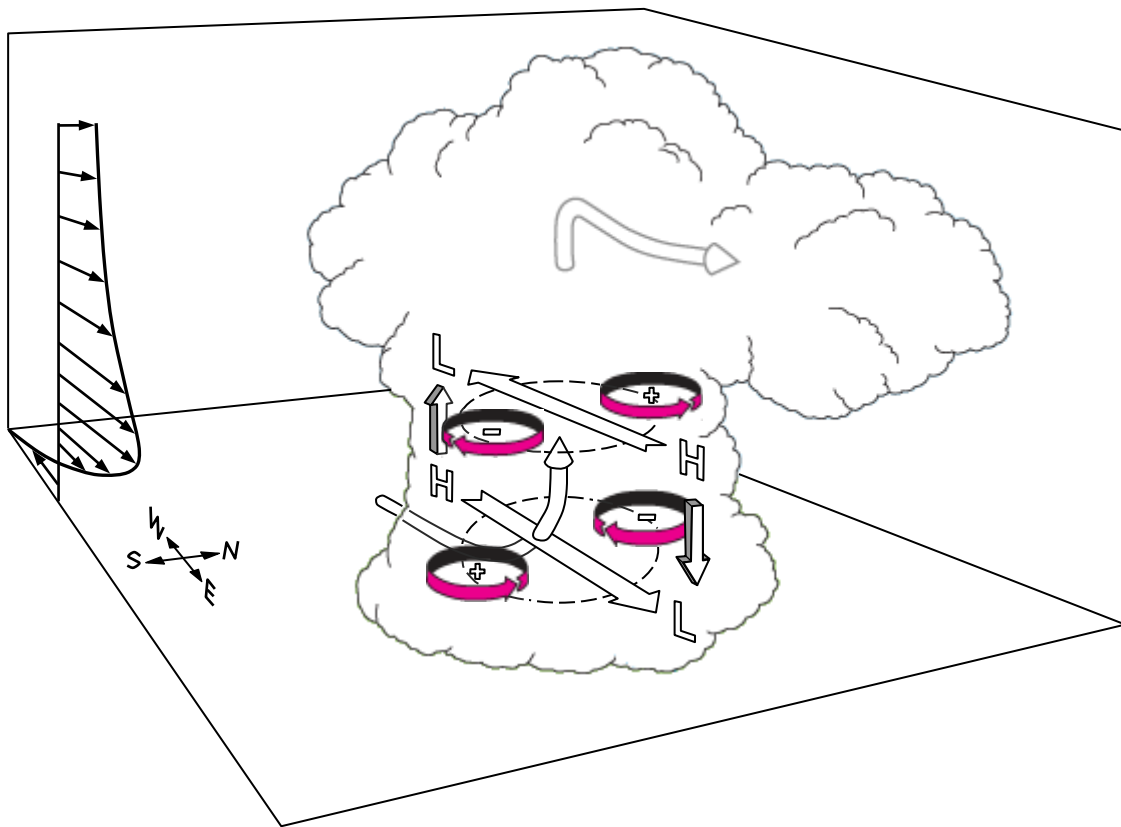
1 Figure 3. (a) The composite of radar VMI reflectivity (dBZ, scale on the right) near Taiwan
 2 overlaid with the ECMWF-YOTC 850 hPa horizontal winds [m s^{-1} , full (half) barb = 10 (5) m
 3 s^{-1}] at 06:00 UTC 8 August 2009. The TC center is marked by the typhoon symbol, and the 1
 4 km domain used in this study is also plotted (black dotted region). The triangle marks the
 5 location of Chigu radar. (b) Radar VMI reflectivity composites (dBZ, scale at bottom) over
 6 the brown dashed box in (a) every 2 h over 00:00-12:00 UTC 8 August and 00:00-08:00 UTC
 7 9 August 2009.



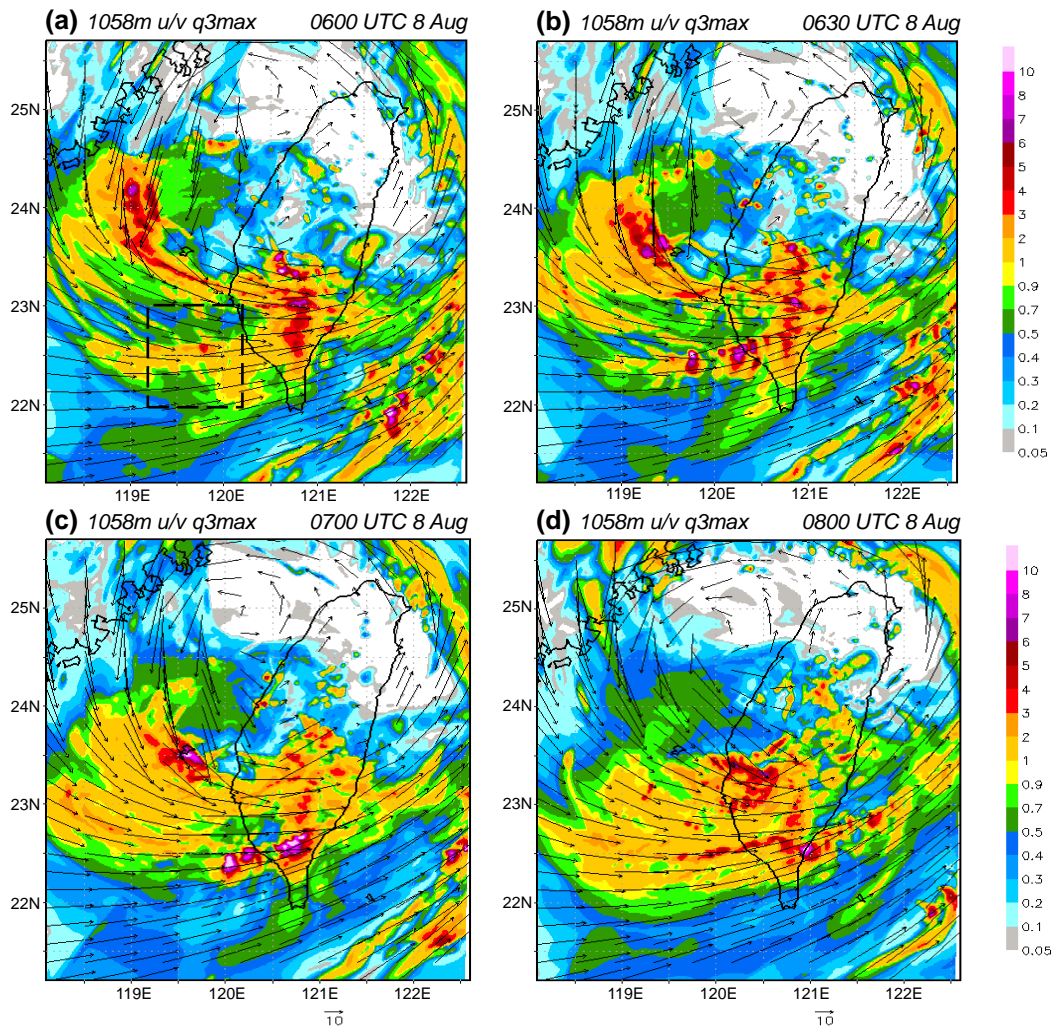
1 Figure 4. Series of CAPPI reflectivity (dBZ, scale at bottom) at 3 km observed by the Chigu
 2 radar (cf. Fig. 3 for location) every 10 min during 05:10-05:40 and 06:20-06:50 UTC 8
 3 August 2009, for regions of $100 \times 45 \text{ km}^2$ covering the E-W oriented rainbands (courtesy of
 4 Prof. C.-H. Liu). The concentric rings are 20 km apart. Selected back-building cells are
 5 labeled as A-G and cell motions are marked (dashed lines).



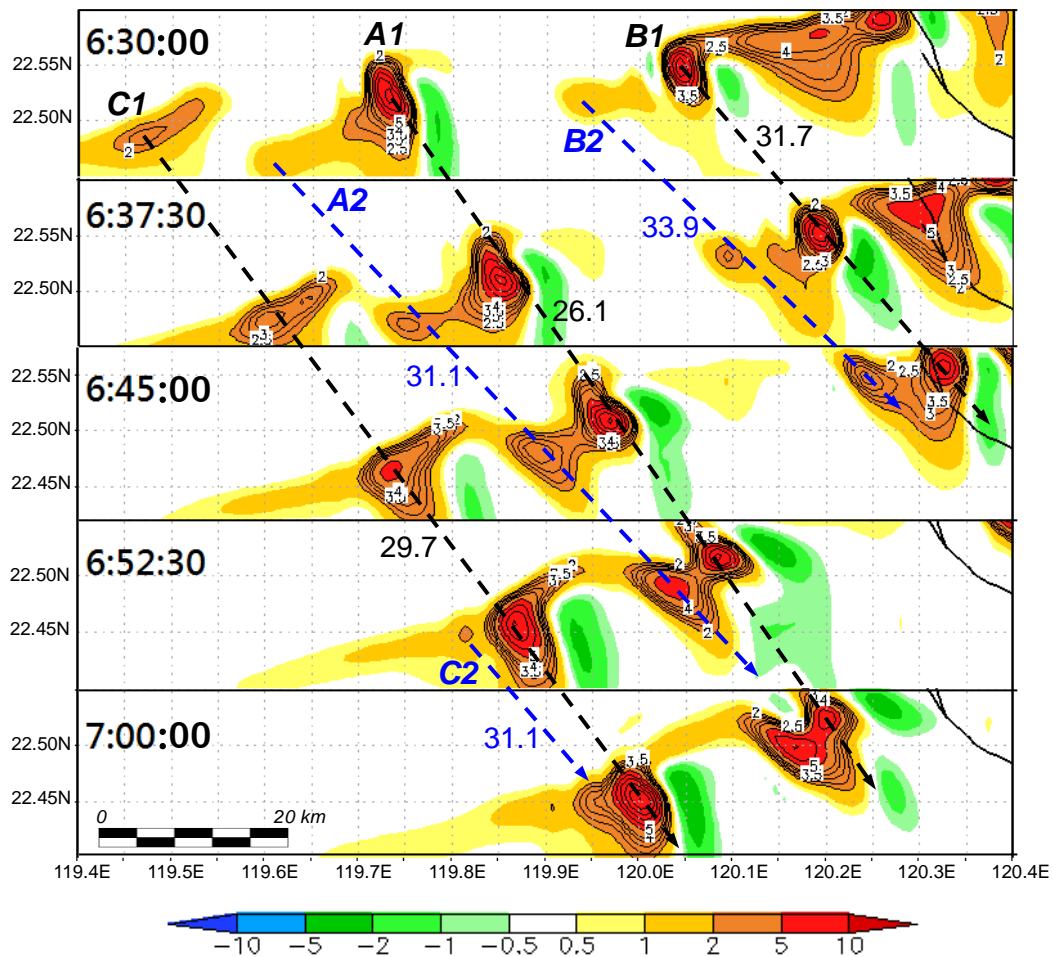
1 Figure 5. Hodograph of the mean wind (m s⁻¹) inside 22-24°N, 118.3-121°E (brown dashed
 2 box in Fig. 3a) computed from the ECMWF-YOTC analyses at (a) 00:00, (b) 06:00, and (c)
 3 12:00 UTC 8 August, 2009. The numbers along the curve indicate pressure (hPa) at nearby
 4 dots.



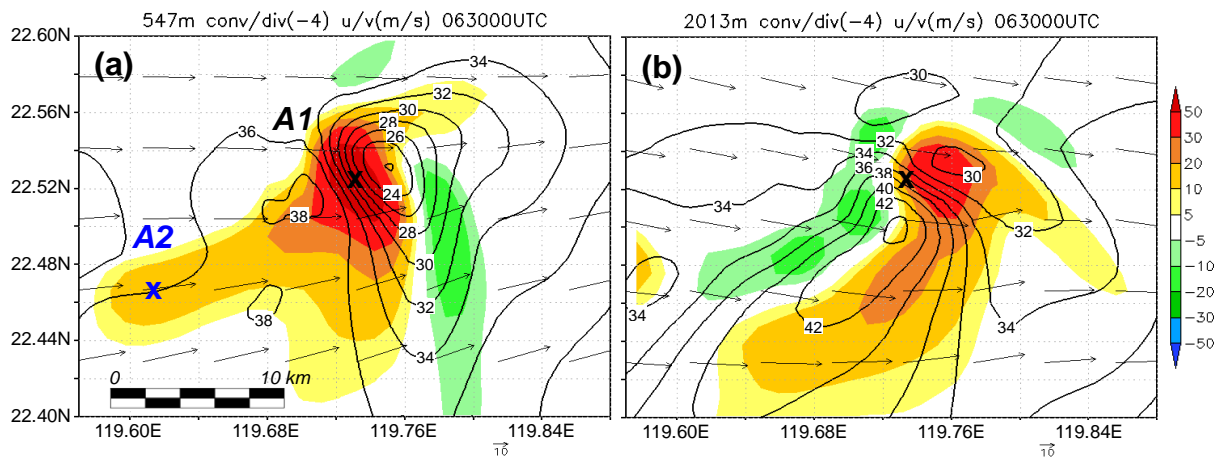
1 Figure 6. A schematic showing the distribution of dynamical pressure perturbations (marked
 2 by “H” for anomalous high and “L” for anomalous low) relative to a mature storm cell in an
 3 environment with the presence of a westerly low-level jet (LLJ) and westerly (easterly)
 4 vertical shear below (above) the jet core as in our case. The configuration is in favor of new
 5 development at the rear side and a slower moving speed of the cell.



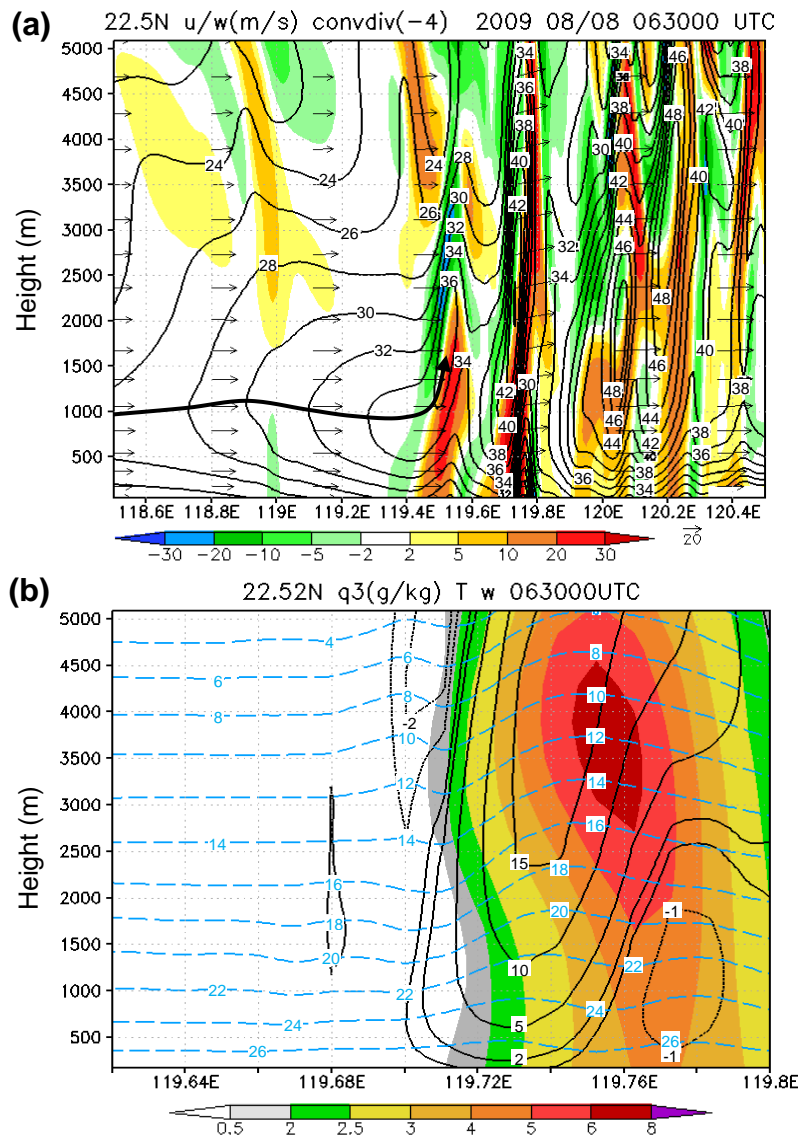
1 Figure 7. Model-simulated column maximum mixing ratio of total precipitating hydrometeors
 2 (g kg^{-1} , rain + snow + graupel, colors, scales on the right) and horizontal winds (m s^{-1} ,
 3 reference vector at bottom) at 1058 m at (a) 06:00 UTC, (b) 06:30 UTC, (c) 07:00 UTC and
 4 (d) 08:00 UTC 8 August 2009 in the 1 km run. The dashed box in (a) depicts the area of
 5 pressure perturbation calculation ($22\text{--}23^\circ\text{N}$, $119.2\text{--}120.2^\circ\text{E}$).



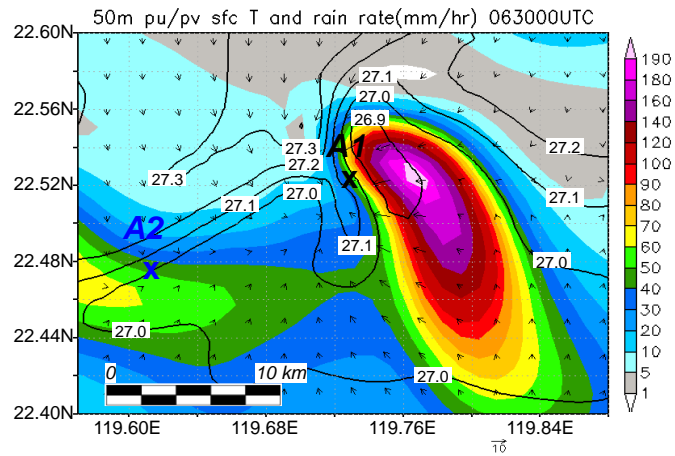
1 Figure 8. Similar to Fig. 4, but showing model-simulated vertical velocity (m s^{-1} , color shades
 2 and contours) at the height of 1058 m (sixth output level) over the period of 06:30-07:00 UTC
 3 (every 7.5 min) 8 August 2009 from the 1 km experiment. Contours start from 2 m s^{-1} , at
 4 intervals of 0.5 (1.0) m s^{-1} up to (above) 4 m s^{-1} . Old cells (A1, B1, and C1) and nearby new
 5 cells (A2, B2, and C2) and their estimated propagation speeds (m s^{-1}) are labeled.



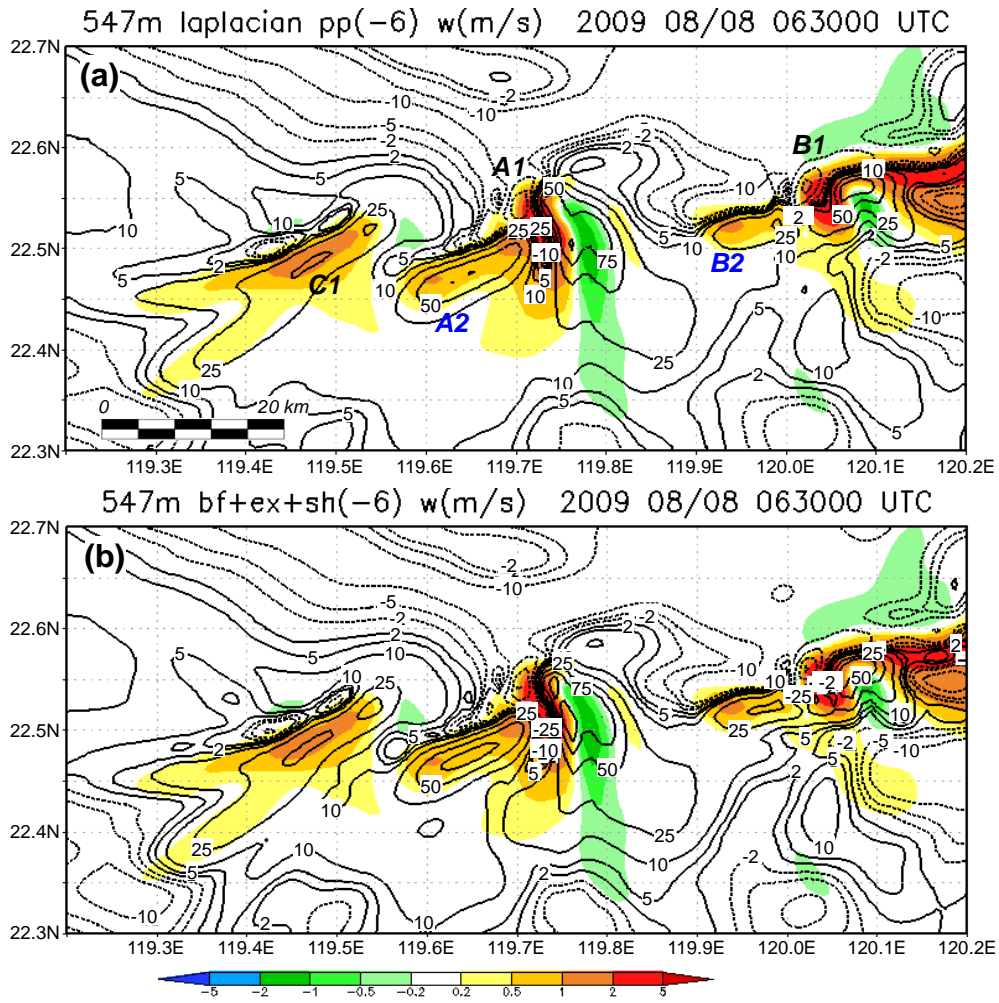
1 Figure 9. Model-simulated horizontal winds (m s^{-1} , vectors, reference vector at bottom), wind
 2 speed (contours, intervals: 2 m s^{-1}), and convergence/divergence (10^{-4} s^{-1} , color, positive for
 3 convergence, scales on the right) at (a) 547 m (fourth output level) and (b) 2013 m (ninth
 4 output level) associated with the convective cell “A1” off the southwestern coast of Taiwan at
 5 06:30 UTC 8 August 2009. The “x” marks the updraft center at 1058 m (cf. Fig. 8).



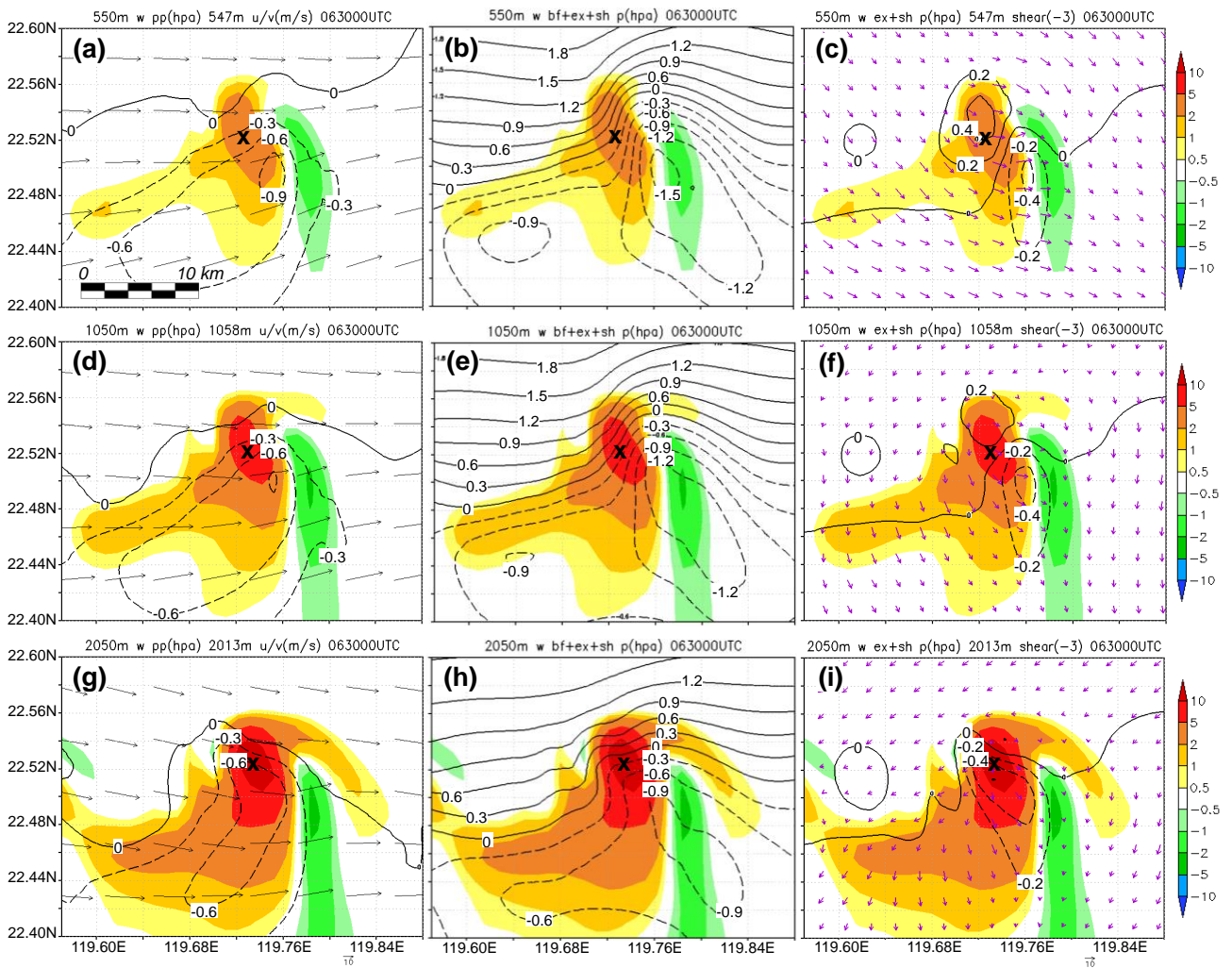
1 Figure 10. E-W vertical cross sections, through cell A1, of model-simulated (a) wind vectors
 2 on the section plane (m s^{-1} , reference vector at bottom), and horizontal wind speed (m s^{-1} ,
 3 isotachs, every 2 m s^{-1}) and convergence/divergence (10^{-4} s^{-1} , color, scale at bottom, positive
 4 for convergence) along 22.5°N from 118.5 to 120.5°E (about 200 km in length), and (b)
 5 vertical velocity (m s^{-1} , contours, at ± 1 , ± 2 , ± 5 , ± 10 , and $\pm 15 \text{ m s}^{-1}$, dotted for downward
 6 motion), temperature ($^\circ\text{C}$, dashed cyan isotherms, every 2°C), and mixing ratio of total
 7 precipitation (g kg^{-1} , color, scale at bottom), along 22.52°N from 119.62 to 119.8°E (about 18
 8 km in length) at $06:30 \text{ UTC}$ $8 \text{ August } 2009$. The thick arrow-line in (a) marks the axis of LLJ
 9 in the background flow.



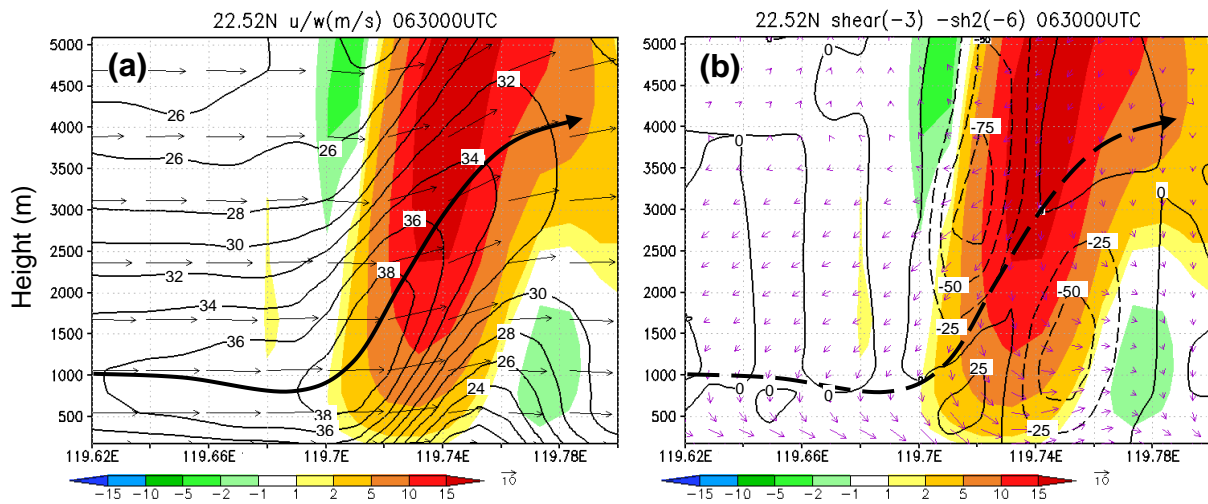
1 Figure 11. As in Fig. 9a, but showing model-simulated surface air temperature ($^{\circ}\text{C}$, contours,
 2 intervals: 0.1°C), horizontal wind perturbation (u', v') at 50 m (m s^{-1} , vectors, reference
 3 vector at bottom), and (instantaneous) rainrate (mm h^{-1} , color, scales on the right) at 06:30
 4 UTC 8 August 2009. The “x” marks the updraft/ascending centers of A1 and A2 at 50 m.



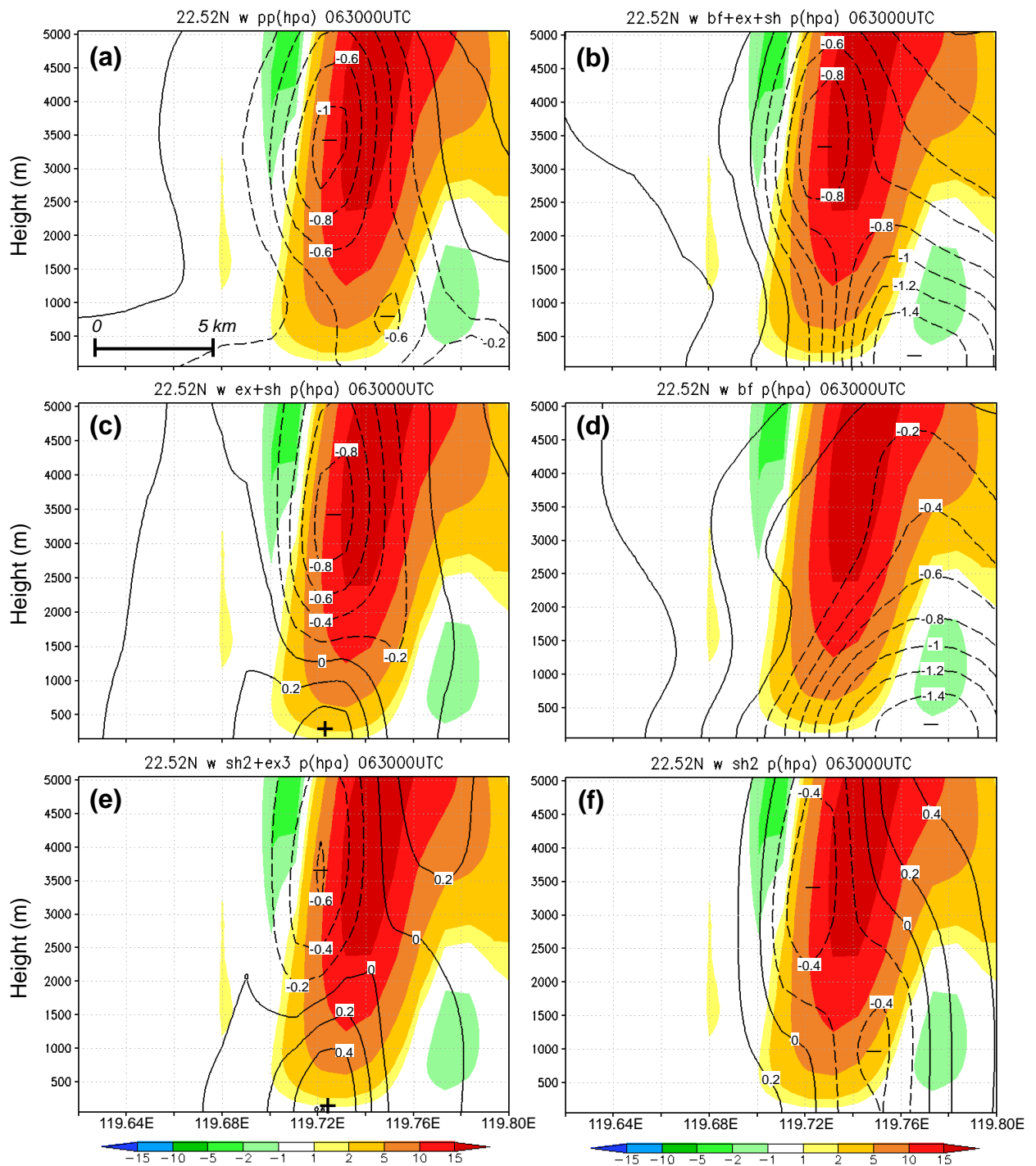
1 Figure 12. Model-simulated w (m s^{-1} , color, scales at bottom) and (a) $\nabla^2 p'$ ($10^{-6} \text{ Pa m}^{-2}$,
2 contours, dashed for negative values) computed from p' using the separation method and (b)
3 $\nabla^2 p'_b + \nabla^2 p'_d$ obtained by adding all the rhs terms in Eqs. (11) and (13) together, at 547 m at
4 06:30 UTC 8 August 2009. Contour levels are at ± 2 , ± 5 , ± 10 , ± 25 , ± 50 , ± 75 , and $\pm 100 \times 10^{-6}$
5 Pa m^{-2} , respectively, and are the same in (a, b). The cells are labeled as in Fig. 8.



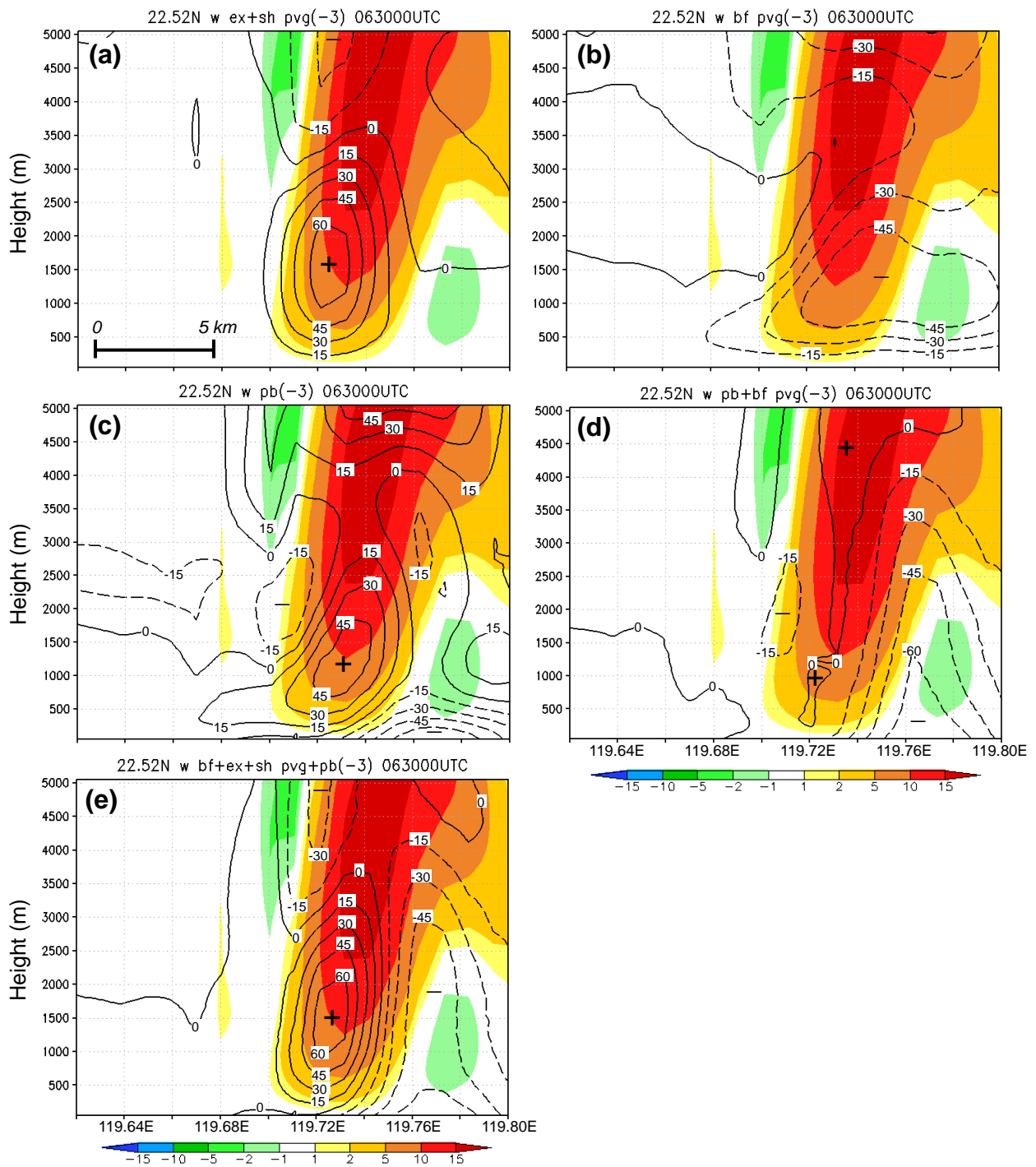
1 Figure 13. Model-simulated w (m s^{-1} , color, scales on the right) and (a) total p' (hPa, contours,
 2 every 0.3 hPa, dashed for negative values) and horizontal winds (m s^{-1} , vectors, reference
 3 vector at bottom), (b) $p'_b + p'_d$ (hPa, contours) solved by the relaxation method, and (c) p'_d
 4 (hPa, contours, every 0.2 hPa) solved by the relaxation method and vertical wind shear (10^{-3}
 5 s^{-1} , purple vectors, reference vector at bottom) at 550 m at 06:30 UTC 8 August 2009. (d-f)
 6 and (g-i) as in (a-c), except at 1050 and 2050 m, respectively. For horizontal wind and vertical
 7 wind shear, vectors at the closest model output level (547, 1058, and 2013 m, respectively)
 8 are plotted, and the “x” marks the updraft center in each panel.



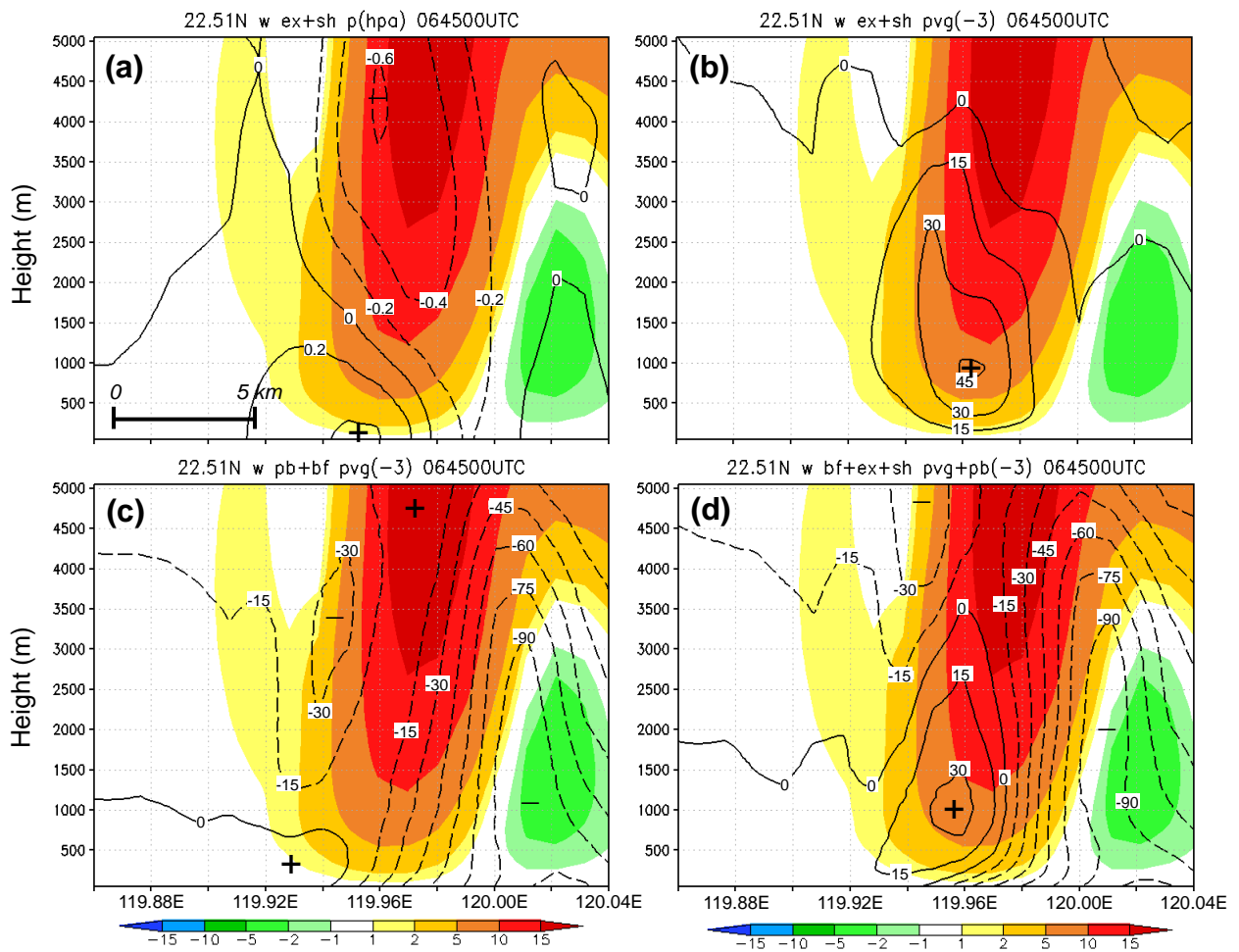
1 Figure 14. E-W vertical cross sections, through cell A1, of model-simulated w (m s^{-1} , color,
 2 scale at bottom) and (a) wind vectors on the section plane (m s^{-1} , reference vector at bottom),
 3 and u -wind speed (m s^{-1} , isotachs, every 2 m s^{-1}) and (b) vertical wind shear (10^{-3} s^{-1} , purple
 4 vectors, reference vector at bottom) and -1 times the x -component of shearing term in Eq. (13)
 5 ($10^{-6} \text{ Pa m}^{-2}$, every $25 \times 10^{-6} \text{ Pa m}^{-2}$, dashed for negative values) along 22.52°N from 119.62
 6 to 119.8°E (about 18 km in length) at $06:30 \text{ UTC}$ $8 \text{ August } 2009$. The thick (dashed) arrow
 7 lines in (a) and (b) mark the axis of LLJ.



1 Figure 15. As in Fig. 14, except for w (m s^{-1} , color, scale at bottom) and (a) total p' (hPa,
 2 contours, every 0.2 hPa, dashed for negative values) separated from the background, and (b)
 3 $p'_b + p'_d$, (c) p'_d , (d) p'_b , (e) the portion of p'_d from SH2 and EX3, and (f) the portion of p'_d
 4 from SH2 alone (all in hPa, contours) in Eq. (13) solved by the relaxation method. The
 5 positive and negative centers are labeled by plus and minus signs, respectively.



1 Figure 16. As in Fig. 14, except for w (m s^{-1} , color, scale at bottom) and the vertical (z)
 2 component of perturbation pressure gradient force (10^{-3} m s^{-2} , contours, every $15 \times 10^{-3} \text{ m s}^{-2}$,
 3 dashed for negative values) from (a) p'_d , (b) p'_b , (c) buoyancy (B), (d) $p'_b + B$, and (e) $p'_d +$
 4 $p'_b + B$, respectively. The positive and negative centers are labeled by plus and minus signs,
 5 respectively.



1 Figure 17. (a) As in Fig. 15c, except for w (m s^{-1} , color) and p'_d (hPa, contours, every 0.2 hPa)
 2 along 22.51°N from 119.86 to 120.04°E (about 18 km in length) at 06:45 UTC 8 August 2009.
 3 (b)-(d) As in Fig. 16, except for w and the z -component of perturbation pressure gradient force
 4 (10^{-3} m s^{-2} , contours, every $15 \times 10^{-3} \text{ m s}^{-2}$) from (b) p'_d , (c) $p'_b + B$, and (d) $p'_d + p'_b + B$,
 5 respectively, at 06:45 UTC along the same cross-section as (a).